Geometrically non-linear 3D finite-element analysis of micropolar continuum

Sara Grbčić Erdelj[a], Gordan Jelenić[a,*], Adnan Ibrahimbegović[b]

[a] *University of Rijeka, Faculty of Civil Engineering, Croatia*
[b] *Université de Technologie de Compiègne - Sorbonne Universités, France*

Abstract

In this work a 3D geometrically non-linear micropolar finite element formulation based on Biot-like tensor representation of stresses, couple stresses, strains and curvature is presented. The discrete approximation is based on hexahedral finite elements with Lagrange interpolation for displacements and rotational spins. The complete residual derivation, linearisation and update are presented in detail. The elements are tested against a non-linear generalisation of the linear micropolar pure-bending problem, derived in this work, and it is shown that the elements converge to the derived solution. The elements are additionally tested on a combined bending and torsion problem and a well-known 45° bend as a genuine problem involving large 3D rotations, both also analysed in the framework of micropolar elasticity. It is observed that the derived finite elements are reliable and robust in modelling finite deformation problems in micropolar elasticity, exhibiting large displacements and large rotations and converge to reference geometrically non-linear classical elasticity solutions for small micropolar effects. With increasing micropolar effects the response becomes stiffer and the presented numerical examples may serve as benchmark problems to test geometrically non-linear micropolar finite elements including those involving large 3D rotations.

*Corresponding author
Email addresses: sara.grbcic@uniri.hr (Sara Grbčić Erdelj), gordan.jelenic@uniri.hr (Gordan Jelenić), adnan.ibrahimbegovic@utc.fr (Adnan Ibrahimbegović)

Keywords: micropolar theory, finite element method, geometrical non-linearity, non-linear pure bending, 45°-bend cantilever, micropolar benchmark problems

1. Introduction

In the vast majority of engineering practical applications the classical (Cauchy) theory of continuum mechanics manages to describe the material behaviour faithfully, especially for highly homogeneous materials such as metals, where any microstructure scale is negligible compared to a representative specimen scale. However, artificial lightweight materials, such as lightweight concrete, modern foams and polymers, honeycomb materials etc. characterised by non-negligible length-scale/specimen-scale ratio are becoming increasingly omnipresent. In such materials, smaller specimens have an increased stiffness (referred to as the *size-effect* phenomenon), an effect not present in the classical continuum theory, which necessitates application of *alternative* continuum theories such as the *micropolar* (or Cosserat) theory [1].

This theory is capable of capturing the length-scale effects due to an additional kinematic field (orientation) present in the actual formulation. The theory itself is widely known (see e.g. [2, 3, 4] among many other sources), but due to the lack of reliable procedures to determine experimentally the additional material parameters present, it is still not widely used in the analysis and design of structures. Nevertheless, micropolar constitutive behaviour has been numerically analysed in a variety of linear finite element formulations, see e.g. [5, 6, 7, 8, 9, 10, 11, 12, 13, 14], as just a part of an extensive list of references concerned with finite-element implementation of linear micropolar models. However, linear micropolar models are not always appropriate for realistic description of a structural response.

In the non-linear regime, the theory has been extensively analysed in [3, 15, 16, 17, 18], but its numerical implementation is not as broadly given. This is particularly the case for 3D applications, where the first and only finite-element implementation familiar to us which deals with pure micropolar geometrical non-linearity is the work of Bauer et al. [19]. Still, as no non-linear representative solutions exist, mostly linear benchmark problems have been considered and run in the non-linear regime. The formulation has been extended to material non-linearity in [20] and [21] where the authors have analysed micropolar hyperelasticity and hyper-elastoplasticity and focused their attention on those effects. However, a set of representative problems to test the micropolar geometrical non-linearity is still missing.

In the scope of this work we limit our attention to geometric non-linearity and focus on linear elastic bodies, which, when deformed, exhibit large displacements and large rotations in 3D space. The 3D finite rotations, in particular are *non-additive* and *multiplicatively non-commutative* and as such require a special mathematical treatment. This is significantly more complex than the corresponding treatment of displacements and is in this paper addressed in detail with special emphasis on numerical implementation using hexahedral finite elements with Lagrange interpolation. The demanding linearisation procedure of the element residual force vector, as well as the update process in the iterative Newton–Raphson solution procedure, in particular, are presented in all the necessary detail. The finite elements developed are tested on three numerical examples encompassing pure bending, torsion and a genuine large 3D deformation problem involving large rotations, which we propose as a set of geometrically non-linear micropolar benchmark problems.

2. Non-linear micropolar continuum model

Governing equations of a geometrically non-linear micropolar continuum model are presented here. The detailed derivation of the approach can be found in [22], including its linear form. More detail on geometrically non-linear micropolar models, among other sources, may be found in [17, 23, 24, 19].

2.1. Strong form of equilibrium equations

Consider an undeformed body occupying the domain $\mathcal{B}_0$ in the three-dimensional Euclidean space $\mathbb{E}$ that deforms to a new placement $\mathcal{B}$, as shown in Figure 1. In the reference placement, taken to be the undeformed state at time $t = 0$, each material point of a micropolar continuum is defined by its position vector

$\mathbf{X} = X_i\mathbf{E}_i$ relative to the origin (with $\{\mathbf{E}_i\}$, $i = 1,2,3$ as right-handed orthonormal base vectors) and by three right-handed orthonormal vectors $\{\mathbf{W}_i\}$, defining the *orientation* of the material point. In a deformed placement $\mathcal{B}$ at time t the position of the same particle is now defined by another position vector $\mathbf{x} = x_i\mathbf{e}_i$ relative to the origin (with $\{\mathbf{e}_i\} = \{\mathbf{E}_i\}$), while its orientation is defined by three new right-handed orthonormal vectors $\{\mathbf{k}_i\}$. Even though the vector bases $\mathbf{E}_i$ and $\mathbf{e}_i$ are here taken to be equal [25], we keep notational distinction between them and call the fields defined over $\mathcal{B}_0$ *material* (written in upper-case) and those defined over $\mathcal{B}$ *spatial* (written in lower-case).

The relation between the two orientations is defined as $\mathbf{k}_i = \mathbf{Q}\mathbf{W}_i$, with $\mathbf{Q}$ being a proper orthogonal *microrotation* tensor which belongs to the so-called special orthogonal rotation group SO(3) such that it satisfies $\mathbf{Q}^{-1} = \mathbf{Q}^{\mathrm{T}}$, $\det\mathbf{Q} = +1$ and $\mathbf{Q} = \exp\widehat{\boldsymbol{\vartheta}}$, where $\widehat{\boldsymbol{\vartheta}}$ is a skew-symmetric tensor belonging to Lie algebra so(3) such that $\widehat{\boldsymbol{\vartheta}}\mathbf{v} = \boldsymbol{\vartheta} \times \mathbf{v}$ for any 3D vector $\mathbf{v}$ and $\boldsymbol{\vartheta}$ is the 3D *microrotation* vector. More on SO(3) and so(3) can be found e.g. in [26].

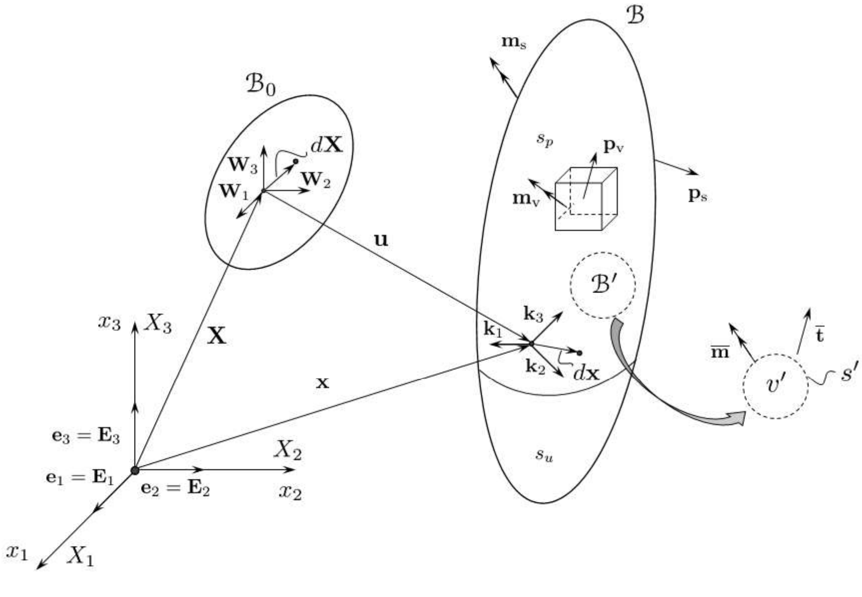

Figure 1: Initial and deformed configuration of a micropolar body in Euclidean space

Let the body $\mathcal{B}$ be subject to distributed loadings $\mathbf{p}_{\mathrm{v}}$ as a specific body force, $\mathbf{m}_{\mathrm{v}}$ as a specific body moment, $\mathbf{p}_{\mathrm{s}}$ as a specific surface force and $\mathbf{m}_{\mathrm{s}}$ as a specific surface moment, as shown in Figure 1. The body surface s is divided into two parts: s_p with prescribed loading and s_u with prescribed displacements and rotations. We analyse an arbitrary part of the body, denoted as $\mathcal{B}'$ of a volume v' and with a closed surface s' in the deformed configuration. According to *Cauchy's theorem* (see e.g. [27]) there exist a mean stress vector $\overline{\mathbf{t}}$ and a mean couple-stress vector $\overline{\mathbf{m}}$ on s', which for infinitesimally small $\mathcal{B}'$ become the *stress vector field* $\mathbf{t} = \boldsymbol{\sigma}\mathbf{n}$ and the *couple-stress vector field* $\mathbf{m} = \boldsymbol{\mu}\mathbf{n}$, with $\mathbf{n}$ as the outward unit normal on s', $\boldsymbol{\sigma}$ as the true (Cauchy) *stress tensor field* and $\boldsymbol{\mu}$ as the corresponding *couple-stress tensor field*, both of them generally non-symmetric. The strong form of the force and moment equilibrium on $\mathcal{B}$ thus follows as

$$\mathbf{p}_{\mathrm{v}} + \mathrm{div}\ \boldsymbol{\sigma} = \mathbf{0}, \tag{1}$$

$$\mathrm{div}\ \boldsymbol{\mu} + \mathrm{ax}(\boldsymbol{\sigma} - \boldsymbol{\sigma}^{\mathrm{T}}) + \mathbf{m}_{\mathrm{v}} = \mathbf{0}, \tag{2}$$

with the corresponding natural boundary conditions as

$$\boldsymbol{\sigma}\ \mathbf{n} = \mathbf{p}_{\mathrm{s}}, \quad \boldsymbol{\mu}\ \mathbf{n} = \mathbf{m}_{\mathrm{s}} \ \text{ on } s_p. \tag{3}$$

Here and throughout the paper the divergence operator of a second-order tensor field $\mathbf{A}$ is defined as $\mathrm{div}\ \mathbf{A} = \mathbf{A}\nabla_x$ where $\nabla_x = \dfrac{\partial}{\partial x_i}\mathbf{e}_i$. The axial operator ax in (2) extracts the so-called axial vector of a skew-symmetric tensor, i.e. $\mathrm{ax}(\boldsymbol{\sigma} - \boldsymbol{\sigma}^{\mathrm{T}}) = \langle \sigma_{32} - \sigma_{23} \quad -\sigma_{31} + \sigma_{13} \quad \sigma_{21} - \sigma_{12} \rangle^{\mathrm{T}}$. Although equilibrium equations (1) and (2) have the same form as those in the linear analysis (see e.g. [13]), the problem remains non-linear, because the domain v and its boundary s are now unknown depending on the displacement field. In order to find the solution of our problem we now transform (1) and (2) in order to re-express them over a known configuration.

The relation between an infinitesimal change in positions $d\mathbf{x}$ and $d\mathbf{X}$ is described by the so-called *deformation gradient* $\mathbf{F} = \mathbf{F}(\mathbf{X}, t)$ as $d\mathbf{x} = \mathbf{F}\, d\mathbf{X}$ where $\mathbf{F} = \text{GRAD}\ \mathbf{x} = \mathbf{x} \otimes \nabla_X$, with $\nabla_X = \dfrac{\partial}{\partial X_i}\mathbf{E}_i$ or $\mathbf{F} = \mathbf{x}\nabla_X^{\mathrm{T}}$. The deformation gradient tensor also describes the transformation of an infinitesimal surface dS into ds and an infinitesimal volume dV into dv during the deformation via $ds\mathbf{n} = (\det\mathbf{F}\ \mathbf{F}^{-\mathrm{T}})dS\mathbf{N} = dS(\text{cof}\ \mathbf{F})\mathbf{N}$ (the so-called Nanson formula, see e.g. [25]) and $dv = JdV = \det\mathbf{F}dV$, where $\mathbf{n}$ and $\mathbf{N}$ represent the surface normals in the spatial and material configuration, respectively.

By expressing (1) and (2) in a weak form and applying the change of variables theorem [28] we obtain the strong form of the equilibrium equations on $\mathcal{B}_0$ as [22]

$$\text{DIV}(\mathbf{QB}) + \mathbf{P}_{\mathrm{V}} = \mathbf{0}, \tag{4}$$

$$\text{DIV}(\mathbf{QG}) + \text{ax}(\mathbf{QBF}^{\mathrm{T}} - \mathbf{FB}^{\mathrm{T}}\mathbf{Q}^{\mathrm{T}}) + \mathbf{M}_{\mathrm{V}} = \mathbf{0}, \tag{5}$$

with the boundary conditions on S_p

$$(\mathbf{QB})\mathbf{N} = \mathbf{P}_{\mathrm{S}} \quad \text{and} \quad (\mathbf{QG})\mathbf{N} = \mathbf{M}_{\mathrm{S}}. \tag{6}$$

Here, $\mathbf{B} = J\mathbf{Q}^{\mathrm{T}}\boldsymbol{\sigma}\mathbf{F}^{-\mathrm{T}} = B_{IJ}\mathbf{E}_i \otimes \mathbf{E}_j$ and $\mathbf{G} = J\mathbf{Q}^{\mathrm{T}}\boldsymbol{\mu}\mathbf{F}^{-\mathrm{T}} = G_{IJ}\mathbf{E}_i \otimes \mathbf{E}_j$ represent the Biot-like stress and couple stress tensors (the '-like' part coming as a result of the definition in which we have the microrotation tensor $\mathbf{Q}$, rather than the rotation tensor from the polar decomposition of the deformation gradient), while $\mathbf{P}_{\mathrm{V}}$, $\mathbf{M}_{\mathrm{V}}$, $\mathbf{P}_{\mathrm{S}}$ and $\mathbf{M}_{\mathrm{S}}$ represent body and surface loadings per unit of undeformed volume/area.

2.2. Non-linear kinematic equations

To derive the non-linear strain tensors, we enforce the equivalence between the strong and weak forms of the equilibrium equations following Reissner's approach [29]. Firstly, we assume that there exist virtual work-conjugate Biot-like strain tensors $\overline{\mathbf{E}}$ and $\overline{\mathbf{K}}$ to the existing Biot-like stress tensors $\mathbf{B}$ and $\mathbf{G}$. The virtual work equation is given as

$$V_i - Ve = \int_V \left(\overline{\mathbf{E}} : \mathbf{B} + \overline{\mathbf{K}} : \mathbf{G}\right) dV - \int_V \left(\overline{\mathbf{u}} \cdot \mathbf{P}_{\mathrm{V}} + \overline{\boldsymbol{\varphi}} \cdot \mathbf{M}_{\mathrm{V}}\right) dV$$
$$- \int_{S_p} \left(\overline{\mathbf{u}} \cdot \mathbf{P}_{\mathrm{S}} + \overline{\boldsymbol{\varphi}} \cdot \mathbf{M}_{\mathrm{S}}\right) dS = 0, \tag{7}$$

where $\overline{\mathbf{E}}$ represents the virtual micropolar Biot-like strain tensor and $\overline{\mathbf{K}}$ represents the virtual Biot-like curvature tensor, while $\overline{\mathbf{u}}$ and $\overline{\boldsymbol{\varphi}}$ are kinematically admissible virtual displacement and virtual microrotation fields obtained from a perturbed configuration

$$\mathbf{x}_\epsilon = \mathbf{x} + \epsilon\overline{\mathbf{u}}, \quad \mathbf{Q}_\epsilon = \exp(\epsilon\widehat{\overline{\boldsymbol{\varphi}}})\mathbf{Q}$$

as

$$\overline{\mathbf{u}} = \left.\frac{\mathrm{d}}{\mathrm{d}\epsilon}\right|_{\epsilon=0} \mathbf{x}_\epsilon \quad \text{and} \quad \widehat{\overline{\boldsymbol{\varphi}}}\mathbf{Q} = \left.\frac{\mathrm{d}}{\mathrm{d}\epsilon}\right|_{\epsilon=0} \mathbf{Q}_\epsilon.$$

The dot products between tensor quantities are defined in AppendixB. Substituting (4)-(6) in (7) and applying some mathematical manipulations gives virtual Biot-like strain and curvature tensors

$$\overline{\mathbf{E}} = \mathbf{Q}^{\mathrm{T}}(\mathrm{GRAD}\overline{\mathbf{u}} + \widehat{\overline{\boldsymbol{\varphi}}}^{\mathrm{T}}\mathbf{F}), \quad \overline{\mathbf{K}} = \mathbf{Q}^{\mathrm{T}}\mathrm{GRAD}\overline{\boldsymbol{\varphi}}, \tag{8}$$

which are equivalent to (13) and (15) in [20]. By integrating (8) and introducing the initial (undeformed) conditions $\mathbf{E}_0 = \mathbf{K}_0 = \mathbf{0}$, we obtain the Biot-like translational strain tensor as

$$\mathbf{E} = \mathbf{Q}^{\mathrm{T}}\mathbf{F} - \mathbf{I}, \tag{9}$$

and the Biot-like curvature tensor as

$$\mathbf{K} = -\frac{1}{2}\boldsymbol{\epsilon} : \left(\mathbf{Q}^{\mathrm{T}}\mathrm{GRAD}\mathbf{Q}\right), \tag{10}$$

or $\mathbf{K} = \mathbf{K}_i \otimes \mathbf{E}_i$ with $\mathbf{K}_i = \text{ax}\left(\mathbf{Q}^{\mathrm{T}} \dfrac{\partial \mathbf{Q}}{\partial X_i}\right)$, where $\boldsymbol{\epsilon} = \epsilon_{ijk} \mathbf{E}_i \otimes \mathbf{E}_j \otimes \mathbf{E}_k$ is the so-called permutation tensor, in which $\epsilon_{ijk} = 1$ if (i, j, k) is a cyclic permutation of $(1, 2, 3)$, $\epsilon_{ijk} = -1$ if (i, j, k) is an anti-cyclic permutation of $(1, 2, 3)$ and $\epsilon_{ijk} = 0$ otherwise.

The derived Biot-like strain tensors coincide with the micropolar material strain measures derived in [17], where the strain tensor is referred to as the stretch tensor, while the curvature tensor is referred to as the wryness tensor and in [19] (equations (13) and (14)) where the strain tensor is referred to as the micropolar Lagrangian strain tensor, while the curvature tensor is referred to as the micropolar Lagrangian curvature tensor. When the Biot-like strain tensors are reduced to 1D, the material strain measures of the geometrically exact 3D beam theory are obtained [30].

2.3. Constitutive equations

In the scope of this work only geometric non-linearity is analysed, keeping the constitutive equations linear and isotropic i.e.

$$\mathbf{B} = \lambda(\text{tr } \mathbf{E})\mathbf{I} + (\mu + \nu)\mathbf{E} + (\mu - \nu)\mathbf{E}^{\mathrm{T}} = \boldsymbol{\mathcal{T}} : \mathbf{E}. \tag{11}$$

where $\text{tr } \mathbf{E} = \mathbf{I} : \mathbf{E}$ and the constitutive tensor $\boldsymbol{\mathcal{T}}$ is given as

$$\boldsymbol{\mathcal{T}} = \lambda \; \mathbf{I} \otimes \mathbf{I} + (\mu + \nu)\boldsymbol{\mathcal{I}} + (\mu - \nu)\boldsymbol{\mathcal{I}}^{\mathrm{T}}, \tag{12}$$

with $\mathbf{I} = \delta_{ij} \mathbf{E}_i \otimes \mathbf{E}_j$ as a second order identity tensor, $\boldsymbol{\mathcal{I}} = \delta_{ik}\delta_{jl} \mathbf{E}_i \otimes \mathbf{E}_j \otimes \mathbf{E}_k \otimes \mathbf{E}_l$ as a fourth order identity tensor and $\boldsymbol{\mathcal{I}}^{\mathrm{T}} = \delta_{il}\delta_{jk} \mathbf{E}_i \otimes \mathbf{E}_j \otimes \mathbf{E}_k \otimes \mathbf{E}_l$ as its transpose, where $\delta_{ij} = 1$ for $i = j$ and $\delta_{ij} = 0$ otherwise. The material parameters λ and μ are the standard Lamé's constants, while the new material parameter ν takes place to allow for fully isotropic response in the presence of non-symmetric tensors $\mathbf{E}$ and $\mathbf{B}$.

The second constitutive equation likewise follows, where $\mathbf{B}$, $\boldsymbol{\mathcal{T}}$, $\mathbf{E}$, λ, μ, ν

are replaced by $\mathbf{G}$, $\boldsymbol{\mathcal{D}}$, $\mathbf{K}$, α, β, γ, respectively, finally giving

$$\mathbf{G} = \alpha(\mathrm{tr}\ \mathbf{K})\mathbf{I} + (\beta + \gamma)\mathbf{K} + (\beta - \gamma)\mathbf{K}^{\mathrm{T}} = \boldsymbol{\mathcal{D}} : \mathbf{K}, \tag{13}$$

with

$$\boldsymbol{\mathcal{D}} = \alpha\ \mathbf{I} \otimes \mathbf{I} + (\beta + \gamma)\boldsymbol{\mathcal{I}} + (\beta - \gamma)\boldsymbol{\mathcal{I}}^{\mathrm{T}}, \tag{14}$$

and α, β, γ as additional material parameters of micropolar isotropic elasticity. Note that such a material may be said to possess a centro-symmetric strain-energy density of the type $W(\mathbf{E}, \mathbf{G}) = \frac{1}{2}\left(\mathbf{E} : \boldsymbol{\mathcal{T}} : \mathbf{E} + \mathbf{G} : \boldsymbol{\mathcal{D}} : \mathbf{G}\right)$.

The micropolar material parameters are related to a set of engineering (measurable) parameters via [13, 14]:

$$\begin{aligned} \lambda &= \frac{2n\ G}{1-2n}, \qquad \mu = G, \qquad \nu = \frac{G\ N^2}{1-N^2}, \\ \alpha &= \frac{2G\ l_t^2(1-\psi)}{\psi}, \quad \beta = G\ l_t^2, \quad \gamma = G(4l_b^2 - l_t^2), \end{aligned} \tag{15}$$

where G is the shear modulus, n is Poisson's ratio, l_t is the characteristic length for torsion, l_b the characteristic length for bending, $N \in \langle 0, 1\rangle$ the classical-micropolar coupling number and $\psi \in \langle 0, 1.5\rangle$ a polar ratio (which relates the torsional strains in a manner analogous to that in which Poisson's ratio relates the normal strains). Characteristic length variables quantify the influence of the microstructure on the macro-behavior of the material and have the dimension of length. Their values are of an order of magnitude of material particle-, grain- or cell-size, depending on the material microstructure. When N tends to the limit $N = 1$, parameter ν tends to infinity, which is the case of the so-called couple-stress elasticity [31].

Alternatively, for the same material, a so-called spatial description could be employed with a constitutive relationship defined in terms of the first Piola–Kirchhoff-like stress tensor and the deformation gradient (as well as their micropolar counterparts), which would involve the constitutive tensors with the same components as here, but with a mixed (spatial–material) basis. The approach taken in this work is motivated by the desire to retain the fully material constitutive tensors $\boldsymbol{\mathcal{T}}$ and $\boldsymbol{\mathcal{D}}$ in the formulation.

3. Finite-element residual-force vector

We start from the weak form given in (7) and introduce (8) to obtain

$$G(\mathbf{u},\mathbf{Q},\overline{\mathbf{u}},\overline{\boldsymbol{\varphi}}) = \int_V \left(\left(\mathbf{Q}^{\mathrm{T}}(\mathrm{GRAD}\overline{\mathbf{u}} + \widehat{\overline{\boldsymbol{\varphi}}}^{\mathrm{T}}\mathbf{F})\right) : \mathbf{B} + (\mathbf{Q}^{\mathrm{T}}\mathrm{GRAD}\overline{\boldsymbol{\varphi}}) : \mathbf{G}\right) dV \\ - \int_V (\overline{\mathbf{u}}\cdot\mathbf{P}_{\mathrm{V}} + \overline{\boldsymbol{\varphi}}\cdot\mathbf{M}_{\mathrm{V}})\, dV - \int_{S_p} (\overline{\mathbf{u}}\cdot\mathbf{P}_{\mathrm{S}} + \overline{\boldsymbol{\varphi}}\cdot\mathbf{M}_{\mathrm{S}})\, dS = 0. \tag{16}$$

The virtual kinematic fields are now approximated as $\overline{\mathbf{u}} \approx \overline{\mathbf{u}}^h$ and $\overline{\boldsymbol{\varphi}} \approx \overline{\boldsymbol{\varphi}}^h$ where $\overline{\mathbf{u}}^h = \mathbf{N}_{\mathbf{u}}\overline{\mathbf{d}}^e$ and $\overline{\boldsymbol{\varphi}}^h = \mathbf{N}_{\varphi}\overline{\mathbf{d}}^e$, and the problem to be solved becomes $G(\mathbf{u},\mathbf{Q},\overline{\mathbf{u}}^h,\overline{\boldsymbol{\varphi}}^h) = 0$. The matrices $\mathbf{N}_{\mathbf{u}}$ and $\mathbf{N}_{\varphi}$ represent the matrices of interpolation functions for the virtual displacement and microrotation fields and $\overline{\mathbf{d}}^e$ represents the virtual vector of element nodal degrees of freedom. For the domain discretisation we employ standard Lagrangian hexahedral finite elements with 8 and 27 nodes, both of which have six degrees of freedom per node, referred to as Hex8NL and Hex27NL. The node-numbering convention is shown in Figure 2 for Hex8NL and in Figure 3 for Hex27NL (presented in three separate images for clarity).

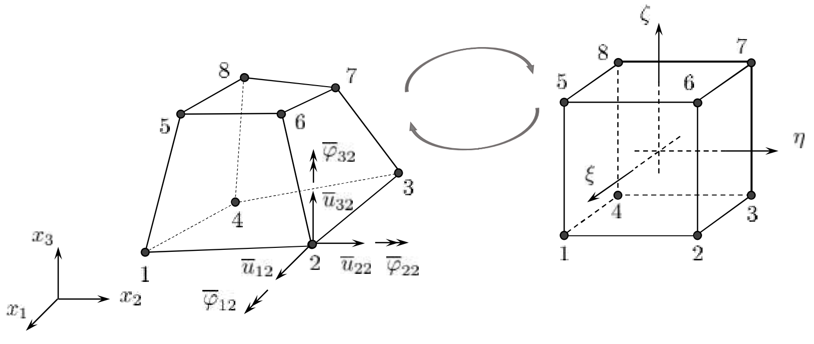

Figure 2: Isoparametric hexahedral finite element with 8 nodes

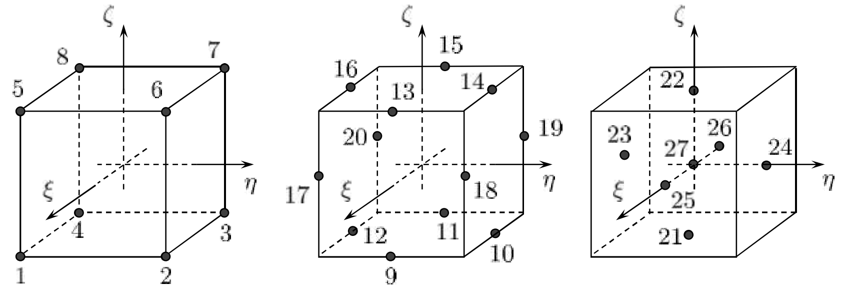

Figure 3: Isoparametric hexahedral finite element with 27 nodes

The virtual vector of element nodal degrees of freedom is defined as

$$\overline{\mathbf{d}}^e = \langle \overline{\mathbf{d}}_1^e \; \overline{\mathbf{d}}_2^e \; \ldots \; \overline{\mathbf{d}}_{n_{node}}^e \rangle,$$

where

$$\overline{\mathbf{d}}_i^e = \left\langle \overline{\mathbf{d}}_{\mathbf{u}_i}^e \overline{\mathbf{d}}_{\boldsymbol{\varphi}_i}^e \right\rangle^{\mathrm{T}} = \langle \overline{u}_{1i} \; \overline{u}_{2i} \; \overline{u}_{3i} \; \overline{\varphi}_{1i} \; \overline{\varphi}_{2i} \; \overline{\varphi}_{3i} \rangle^{\mathrm{T}},$$

i is a node number and n_{node} being equal to either 8 or 27. The matrix interpolation functions are

$$\mathbf{N}_{\mathbf{u}} = [\mathbf{N}_1 \;\; \mathbf{0} \; \ldots \; \mathbf{N}_{n_{node}} \;\; \mathbf{0}] \text{ and } \mathbf{N}_{\varphi} = [\mathbf{0} \;\; \mathbf{N}_1 \ldots \mathbf{0} \;\; \mathbf{N}_{n_{node}}],$$

with $\mathbf{N}_i = N_i \mathbf{I}$. The actual shape functions N_i expressed in terms of the natural co-ordinates ξ, η, ζ ranging from -1 to 1 each (see Figure 2) are given in AppendixA.

The interpolated virtual fields defined in this way are now substituted in $G(\mathbf{u}, \mathbf{Q}, \overline{\mathbf{u}}^h, \overline{\boldsymbol{\varphi}}^h) = 0$ as per (16). Each term in the weak form is shown separately, while step-by-step derivation of all terms is presented in [22]. For the term $\left(\mathbf{Q}^{\mathrm{T}}\mathrm{GRAD}\overline{\mathbf{u}}^h\right) : \mathbf{B}$ we obtain

$$\left(\mathbf{Q}^{\mathrm{T}}\mathrm{GRAD}\overline{\mathbf{u}}^h\right) : \mathbf{B} = \overline{\mathbf{d}}^{e^{\mathrm{T}}} \mathbf{A} \; \mathbf{N}_{\mathbf{u}}{}^{\mathrm{T}} \nabla_X, \tag{17}$$

where $\mathbf{A}$ is a square matrix assembled of $n_{node} \times n_{node}$ 6×6 blocks $\begin{bmatrix} \mathbf{QB} & \mathbf{0} \\ \mathbf{0} & \mathbf{0} \end{bmatrix}$ along the diagonal region and zeros elsewhere. Analogously, we obtain

$$\left(\mathbf{Q}^{\mathrm{T}}\mathrm{GRAD}\overline{\boldsymbol{\varphi}}^{h}\right) : \mathbf{G} = \overline{\mathbf{d}}^{e^{\mathrm{T}}} \mathbf{L}\ \mathbf{N}_{\varphi}{}^{\mathrm{T}}\nabla_X, \tag{18}$$

where $\mathbf{L}$ represents a matrix assembled of $n_{node} \times n_{node}$ 6×6 blocks $\begin{bmatrix} \mathbf{0} & \mathbf{0} \\ \mathbf{0} & \mathbf{QG} \end{bmatrix}$ along the diagonal region and zeros elsewhere. Further, for the term $\left(\mathbf{Q}^{\mathrm{T}}\widehat{\overline{\boldsymbol{\varphi}}^{h}}^{\mathrm{T}}\mathbf{F}\right) : \mathbf{B}$ we obtain

$$\left(\mathbf{Q}^{\mathrm{T}}\widehat{\overline{\boldsymbol{\varphi}}^{h}}^{\mathrm{T}}\mathbf{F}\right) : \mathbf{B} = 2\overline{\mathbf{d}}^{e^{\mathrm{T}}} \mathbf{N}_{\varphi}{}^{\mathrm{T}}\mathrm{ax}\left(\mathrm{skew}\left(\mathbf{F}\mathbf{B}^{\mathrm{T}}\mathbf{Q}^{\mathrm{T}}\right)\right), \tag{19}$$

where $\mathrm{skew}\left(\mathbf{F}\mathbf{B}^{\mathrm{T}}\mathbf{Q}^{\mathrm{T}}\right) = \dfrac{1}{2}\left(\mathbf{F}\mathbf{B}^{\mathrm{T}}\mathbf{Q}^{\mathrm{T}} - \mathbf{QBF}^{\mathrm{T}}\right)$. Thus, the principle of virtual work expressed in terms of interpolated virtual fields only turns into

$$\overline{\mathbf{d}}^{e^{\mathrm{T}}} \mathbf{g}^{e} = 0, \tag{20}$$

where $\mathbf{g}^{e} = \mathbf{q}^{int,e} - \mathbf{q}^{ext,e}$ is the element residual force vector, $\mathbf{q}^{int,e}$ represents the element vector of internal forces and $\mathbf{q}^{ext,e}$ represents the element vector of external forces, given as

$$\mathbf{q}^{int,e} = \int_V \left(\mathbf{A}\ \mathbf{N}_{\mathbf{u}}{}^{\mathrm{T}}\nabla_X + 2\mathbf{N}_{\varphi}{}^{\mathrm{T}}\mathrm{ax}\left(\mathrm{skew}\left(\mathbf{F}\mathbf{B}^{\mathrm{T}}\mathbf{Q}^{\mathrm{T}}\right)\right) + \mathbf{L}\ \mathbf{N}_{\varphi}{}^{\mathrm{T}}\nabla_X\right) dV, \tag{21}$$

$$\mathbf{q}^{ext,e} = \int_V \left(\mathbf{N}_{\mathbf{u}}{}^{\mathrm{T}}\mathbf{P}_{\mathrm{V}} + \mathbf{N}_{\varphi}{}^{\mathrm{T}}\mathbf{M}_{\mathrm{V}}\right) dV + \int_{S_p} \left(\mathbf{N}_{\mathbf{u}}{}^{\mathrm{T}}\mathbf{P}_{\mathrm{S}} + \mathbf{N}_{\varphi}{}^{\mathrm{T}}\mathbf{M}_{\mathrm{S}}\right) dS. \tag{22}$$

The element residual, internal and external force vectors may be expressed as $\mathbf{g}^{e^{\mathrm{T}}} = \left\langle \mathbf{g}_1^{e^{\mathrm{T}}} \ldots \mathbf{g}_{n_{node}}^{e^{\mathrm{T}}} \right\rangle$, $\mathbf{q}^{int,e^{\mathrm{T}}} = \left\langle \mathbf{q}_1^{int,e^{\mathrm{T}}} \ldots \mathbf{q}_{n_{node}}^{int,e^{\mathrm{T}}} \right\rangle$ and $\mathbf{q}^{ext,e^{\mathrm{T}}} = \left\langle \mathbf{q}_1^{ext,e^{\mathrm{T}}} \ldots \mathbf{q}_{n_{node}}^{ext,e^{\mathrm{T}}} \right\rangle$ with their respective nodal contributions following from (17), (18), (19), (B.16) and the structure of $\mathbf{N}_{\mathbf{u}}$ and $\mathbf{N}_{\varphi}$ as

$$\mathbf{g}_i^{e} = \mathbf{q}_i^{int,e} - \mathbf{q}_i^{ext,e}, \tag{23}$$

$$\mathbf{q}_i^{int,e} = \int_V \left\{ \begin{array}{c} \mathbf{QB}(N_i\nabla_X) \\ -N_i\boldsymbol{\epsilon} : (\mathbf{FB}^{\mathrm{T}}\mathbf{Q}^{\mathrm{T}}) + \mathbf{QG}(N_i\nabla_X) \end{array} \right\} dV, \tag{24}$$

$$\mathbf{q}_i^{ext,e} = \int_V \left\{ \begin{array}{c} Ni\mathbf{P}_{\mathrm{V}} \\ Ni\mathbf{M}_{\mathrm{V}} \end{array} \right\} dV + \int_{S_p} \left\{ \begin{array}{c} Ni\mathbf{P}_{\mathrm{S}} \\ Ni\mathbf{M}_{\mathrm{S}} \end{array} \right\} dS. \tag{25}$$

4. Non-linear finite-element solution procedure

To perform the non-linear Newton–Raphson solution procedure the global residual force vector needs to be linearised and equilibrated as follows

$$\begin{aligned} \mathrm{Lin}\,[\mathbf{g}(\mathbf{u},\mathbf{Q})]) &= \mathbf{g}(\mathbf{u},\mathbf{Q}) + \Delta\mathbf{g} \\ &= \mathbf{g}(\mathbf{u},\mathbf{Q}) + \left.\frac{\mathrm{d}}{\mathrm{d}\epsilon}\right|_{\epsilon=0} \mathbf{g}\left(\mathbf{u} + \epsilon\Delta\mathbf{u},\ \exp(\epsilon\widehat{\Delta\boldsymbol{\varphi}})\mathbf{Q}\right) = \mathbf{0}, \end{aligned} \tag{26}$$

where $\mathbf{g} = \underset{e=1}{\overset{n_{elem}}{\mathbb{A}}} \mathbf{g}^e$ with $\mathbb{A}$ as the standard finite-element assembly operator and n_{elem} the total number of finite elements in a mesh, and

$$\left.\frac{\mathrm{d}}{\mathrm{d}\epsilon}\right|_{\epsilon=0} \exp(\epsilon\widehat{\Delta\boldsymbol{\varphi}})\mathbf{Q} = \widehat{\Delta\boldsymbol{\varphi}}\mathbf{Q}. \tag{27}$$

On the element level we thus obtain

$$\mathbf{g}^e(\mathbf{u},\mathbf{Q}) + \Delta\mathbf{g}^e = \mathbf{q}^{int,e} - \mathbf{q}^{ext,e} + \mathbf{K}^e\Delta\mathbf{d}^e, \tag{28}$$

where $\mathbf{K}^e$ to be obtained from $\Delta\mathbf{g}^e = \mathbf{K}^e\Delta\mathbf{d}^e$ represents the element tangent stiffness matrix. To derive $\mathbf{K}^e$ from here we note that

$$\Delta\mathbf{g}^e = \left\{ \begin{array}{c} \Delta\mathbf{g}_1^e \\ \Delta\mathbf{g}_2^e \\ \vdots \\ \Delta\mathbf{g}_{n_{node}}^e \end{array} \right\} = \left\{ \begin{array}{c} \Delta\mathbf{q}_1^{int,e} \\ \Delta\mathbf{q}_2^{int,e} \\ \vdots \\ \Delta\mathbf{q}_{n_{node}}^{int,e} \end{array} \right\}, \tag{29}$$

in which the nodal increment $\Delta\mathbf{g}_i^e$ of the element residual is

$$\Delta\mathbf{g}_i^e = \Delta\mathbf{q}_i^{int,e} = \int \begin{Bmatrix} \Delta\mathbf{g}_i^{e1} \\ \Delta\mathbf{g}_i^{e2} \end{Bmatrix} dV, \tag{30}$$

for the case of constant external loads.

As written in [19], the linearisation process in this case is considered to be highly demanding. In this work, a great effort is made in order to derive the linearised residual and, due to the complexity of the problem, here we want to present the linearisation procedure in a detailed and systematic way.

4.1. Tangent stiffness matrix

The integrands $\Delta\mathbf{g}_i^{e1}$ and $\Delta\mathbf{g}_i^{e2}$ follow from (30), (24), (27), (11) and (13) as

$$\begin{aligned}
\Delta\mathbf{g}_i^{e1} &= \left(\widehat{\Delta\boldsymbol{\varphi}}\mathbf{QB} + \mathbf{Q}\left(\boldsymbol{\mathcal{T}} : \Delta\mathbf{E}\right)\right)(N_i\nabla_X), \\
\Delta\mathbf{g}_i^{e2} &= \left(\widehat{\Delta\boldsymbol{\varphi}}\mathbf{QG} + \mathbf{Q}\left(\boldsymbol{\mathcal{D}} : \Delta\mathbf{K}\right)\right)(N_i\nabla_X) \\
&\quad - N_i\boldsymbol{\epsilon} : \left(\mathrm{GRAD}\Delta\mathbf{u}\mathbf{B}^{\mathrm{T}}\mathbf{Q}^{\mathrm{T}} + \mathbf{F}(\boldsymbol{\mathcal{T}} : \Delta\mathbf{E})^{\mathrm{T}}\mathbf{Q}^{\mathrm{T}} + \mathbf{F}\mathbf{B}^{\mathrm{T}}\mathbf{Q}^{\mathrm{T}}\widehat{\Delta\boldsymbol{\varphi}}^{\mathrm{T}}\right).
\end{aligned} \tag{31}$$

These integrands are analysed in detail in AppendixC.1, AppendixC.2 and AppendixC.3, where the following results are obtained:

$$\begin{aligned}
&\left(\widehat{\Delta\boldsymbol{\varphi}}\mathbf{QB} + \mathbf{Q}\left(\boldsymbol{\mathcal{T}} : \Delta\mathbf{E}\right)\right)(N_i\nabla_X) \\
&= \left(\lambda\mathbf{Q}(N_i\nabla_X)\nabla_X^{\mathrm{T}}\mathbf{Q}^{\mathrm{T}} + (\mu+\nu)\nabla_X^{\mathrm{T}}(N_i\nabla_X)\mathbf{I} + (\mu-\nu)\mathbf{Q}\nabla_X(N_i\nabla_X)^{\mathrm{T}}\mathbf{Q}^{\mathrm{T}}\right)\Delta\mathbf{u} \\
&+ \Big(-\widehat{\mathbf{QB}(N_i\nabla_X)} + \lambda\mathbf{Q}(N_i\nabla_X)2\left[\mathrm{ax}(\mathrm{skew}(\mathbf{F}\mathbf{Q}^{\mathrm{T}}))\right]^{\mathrm{T}} + (\mu+\nu)\widehat{\mathbf{F}(N_i\nabla_X)} \\
&-(\mu-\nu)\mathbf{Q}\mathbf{F}^{\mathrm{T}}\widehat{\mathbf{Q}(N_i\nabla_X)}\Big)\Delta\boldsymbol{\varphi},
\end{aligned} \tag{32}$$

where the free ∇_X in the factor multiplying $\Delta\mathbf{u}$ operates exclusively on $\Delta\mathbf{u}$,

$$
\begin{aligned}
&\left(\widehat{\Delta\varphi}\mathbf{Q}\mathbf{G}+\mathbf{Q}\left(\boldsymbol{\mathcal{D}}:\Delta\mathbf{K}\right)\right)(N_i\nabla_X)\\
&=\Big(-\widehat{\mathbf{Q}\mathbf{G}(N_i\nabla_X)}+\alpha\mathbf{Q}(N_i\nabla_X)\nabla_X^{\mathrm{T}}\mathbf{Q}^{\mathrm{T}}+(\beta+\gamma)\nabla_X^{\mathrm{T}}(N_i\nabla_X)\\
&+(\beta-\gamma)\mathbf{Q}\nabla_X(N_i\nabla_X)^{\mathrm{T}}\mathbf{Q}^{\mathrm{T}}\Big)\Delta\boldsymbol{\varphi},
\end{aligned}
\tag{33}
$$

where the free ∇_X in the factor multiplying $\Delta\boldsymbol{\varphi}$ now operates exclusively on $\Delta\boldsymbol{\varphi}$ and

$$
\begin{aligned}
&-N_i\boldsymbol{\epsilon}:\left(\mathrm{GRAD}\Delta\mathbf{u}\mathbf{B}^{\mathrm{T}}\mathbf{Q}^{\mathrm{T}}+\mathbf{F}(\boldsymbol{\mathcal{T}}:\Delta\mathbf{E})^{\mathrm{T}}\mathbf{Q}^{\mathrm{T}}+\mathbf{F}\mathbf{B}^{\mathrm{T}}\mathbf{Q}^{\mathrm{T}}\widehat{\Delta\boldsymbol{\varphi}}^{\mathrm{T}}\right)\\
&\quad=N_i\widehat{\mathbf{Q}\mathbf{B}\nabla_X}\Delta\mathbf{u}+4\lambda N_i\ \mathrm{ax}(\mathrm{skew}(\mathbf{F}\mathbf{Q}^{\mathrm{T}}))\left[\mathrm{ax}(\mathrm{skew}(\mathbf{F}\mathbf{Q}^{\mathrm{T}}))\right]^{\mathrm{T}}\Delta\boldsymbol{\varphi}\\
&+2\lambda N_i\ \mathrm{ax}(\mathrm{skew}(\mathbf{F}\mathbf{Q}^{\mathrm{T}}))\nabla_X^{\mathrm{T}}\mathbf{Q}^{\mathrm{T}}\Delta\mathbf{u}-(\mu+\nu)N_i\left(\mathbf{F}\mathbf{F}^{\mathrm{T}}-\mathrm{tr}(\mathbf{F}\mathbf{F}^{\mathrm{T}})\mathbf{I}\right)\Delta\boldsymbol{\varphi}\\
&-(\mu+\nu)N_i\widehat{\mathbf{F}\nabla_X}\Delta\mathbf{u}\\
&+(\mu-\nu)N_i\left[\mathbf{m_1}\quad\mathbf{m_2}\quad\mathbf{m_3}\right]\Delta\boldsymbol{\varphi}\\
&+(\mu-\nu)N_i\widehat{\mathbf{Q}\nabla_X}\mathbf{F}\mathbf{Q}^{\mathrm{T}}\Delta\mathbf{u}+N_i\left[\left(\mathbf{F}\mathbf{B}^{\mathrm{T}}\mathbf{Q}^{\mathrm{T}}\right)^{\mathrm{T}}-\mathrm{tr}\left(\mathbf{F}\mathbf{B}^{\mathrm{T}}\mathbf{Q}^{\mathrm{T}}\right)\mathbf{I}\right]\Delta\boldsymbol{\varphi},
\end{aligned}
\tag{34}
$$

where $\mathbf{m_i}=-\mathrm{ax}(2\mathrm{skew}(\mathbf{F}\mathbf{Q}^{\mathrm{T}}\widehat{\mathbf{E}_i}\mathbf{F}\mathbf{Q}^{\mathrm{T}}))$ with $\mathbf{E}_i$ as the material base vectors (see Figure 1) and all ∇_X operate on $\Delta\mathbf{u}$. In this way we derive the integrands $\Delta\mathbf{g}_i^{e1}$ and $\Delta\mathbf{g}_i^{e2}$ in (30) as

$$
\begin{aligned}
&\Delta\mathbf{g}_i^{e1}=-\widehat{\mathbf{Q}\mathbf{B}(N_i\nabla_X)}\Delta\boldsymbol{\varphi}+\lambda\mathbf{Q}(N_i\nabla_X)2\boldsymbol{\ell}^{\mathrm{T}}\Delta\boldsymbol{\varphi}+\lambda\mathbf{Q}(N_i\nabla_X)\nabla_X^{\mathrm{T}}\mathbf{Q}^{\mathrm{T}}\Delta\mathbf{u}\\
&+(\mu+\nu)\widehat{\mathbf{F}(N_i\nabla_X)}\Delta\boldsymbol{\varphi}+(\mu+\nu)\nabla_X^{\mathrm{T}}(N_i\nabla_X)\Delta\mathbf{u}\\
&-(\mu-\nu)\mathbf{Q}\mathbf{F}^{\mathrm{T}}\widehat{\mathbf{Q}(N_i\nabla_X)}\Delta\boldsymbol{\varphi}+(\mu-\nu)\mathbf{Q}
\end{aligned}
\tag{35}
$$

$$
\begin{aligned}
\Delta\mathbf{g}_i^{e2} = &-\widehat{\mathbf{QG}(N_i\nabla_X)}\Delta\boldsymbol{\varphi} + \alpha\mathbf{Q}(N_i\nabla_X)\nabla_X^{\mathrm{T}}\mathbf{Q}^{\mathrm{T}}\Delta\boldsymbol{\varphi} + (\beta+\gamma)\nabla_X^{\mathrm{T}}(N_i\nabla_X)\Delta\boldsymbol{\varphi} \\
&+ (\beta-\gamma)\mathbf{Q}\nabla_X(N_i\nabla_X^{\mathrm{T}})\mathbf{Q}^{\mathrm{T}}\Delta\boldsymbol{\varphi} + N_i\widehat{\mathbf{QB}\nabla_X}\Delta\mathbf{u} + 4\lambda N_i\ \boldsymbol{\ell}\boldsymbol{\ell}^{\mathrm{T}}\Delta\boldsymbol{\varphi} \\
&+ 2\lambda N_i\ \boldsymbol{\ell}\nabla_X^{\mathrm{T}}\mathbf{Q}^{\mathrm{T}}\Delta\mathbf{u} - (\mu+\nu)N_i\left(\mathbf{F}\mathbf{F}^{\mathrm{T}} - \mathrm{tr}(\mathbf{F}\mathbf{F}^{\mathrm{T}})\mathbf{I}\right)\Delta\boldsymbol{\varphi} - (\mu+\nu)N_i\widehat{\mathbf{F}\nabla_X}\Delta\mathbf{u} \\
&+ (\mu-\nu)N_i\left[\mathbf{m_1}\ \mathbf{m_2}\ \mathbf{m_3}\right]\Delta\boldsymbol{\varphi} + (\mu-\nu)N_i\widehat{\mathbf{Q}\nabla_X}\mathbf{F}\mathbf{Q}^{\mathrm{T}}\Delta\mathbf{u} \\
&+ N_i\left[\left(\mathbf{F}\mathbf{B}^{\mathrm{T}}\mathbf{Q}^{\mathrm{T}}\right)^{\mathrm{T}} - \mathrm{tr}\left(\mathbf{F}\mathbf{B}^{\mathrm{T}}\mathbf{Q}^{\mathrm{T}}\right)\mathbf{I}\right]\Delta\boldsymbol{\varphi},
\end{aligned} \tag{36}
$$

where $\boldsymbol{\ell} = \mathrm{ax}(\mathrm{skew}(\mathbf{F}\mathbf{Q}^{\mathrm{T}}))$. It is useful to split the nodal increment $\Delta\mathbf{g}_i^e$ of the element residual $\mathbf{g}^e$ into its geometric and material part as:

$$
\Delta\mathbf{g}_i^e = \Delta\mathbf{g}_{\mathrm{G}_i}^e + \Delta\mathbf{g}_{\mathrm{M}_i}^e, \tag{37}
$$

in which we define the former as the part which depends on the existing stresses and couple stresses. We thus express the geometric part $\Delta\mathbf{g}_{\mathrm{G}_i}^e$ of the nodal residual increment (30), (37) as

$$
\Delta\mathbf{g}_{\mathrm{G}_i}^e = \int_V \begin{Bmatrix} \Delta\mathbf{g}_{\mathrm{G}_i}^{e1} \\ \Delta\mathbf{g}_{\mathrm{G}_i}^{e2} \end{Bmatrix} dV, \tag{38}
$$

where the integrands $\Delta\mathbf{g}_{\mathrm{G}_i}^{e1}$ and $\Delta\mathbf{g}_{\mathrm{G}_i}^{e2}$ follow from (35) and (36) as

$$
\Delta\mathbf{g}_{\mathrm{G}_i}^{e1} = -\widehat{\mathbf{QB}(N_i\nabla_X)}\Delta\boldsymbol{\varphi}, \tag{39}
$$

$$
\begin{aligned}
\Delta\mathbf{g}_{\mathrm{G}_i}^{e2} = &\left(-\widehat{\mathbf{QG}(N_i\nabla_X)} + N_i\left[(\mathbf{F}\mathbf{B}^{\mathrm{T}}\mathbf{Q}^{\mathrm{T}})^{\mathrm{T}} - \mathrm{tr}(\mathbf{F}\mathbf{B}^{\mathrm{T}}\mathbf{Q}^{\mathrm{T}})\mathbf{I}\right]\right)\Delta\boldsymbol{\varphi} \\
&+ N_i\widehat{\mathbf{QB}\nabla_X}\Delta\mathbf{u}.
\end{aligned} \tag{40}
$$

Next we likewise define the material part $\Delta\mathbf{g}_{\mathrm{M}_i}^e$ of the nodal residual increment (30), (37) as

$$
\Delta\mathbf{g}_{\mathrm{M}_i}^e = \int_V \begin{Bmatrix} \Delta\mathbf{g}_{\mathrm{M}_i}^{e1} \\ \Delta\mathbf{g}_{\mathrm{M}_i}^{e2} \end{Bmatrix} dV, \tag{41}
$$

where the integrands $\Delta\mathbf{g}^{e1}_{\mathrm{M}_i}$ and $\Delta\mathbf{g}^{e2}_{\mathrm{M}_i}$ follow from the remaining parts of (35) and (36) as

$$\begin{aligned}\Delta\mathbf{g}^{e1}_{\mathrm{M}_i}=&\big(\lambda\mathbf{Q}(N_i\nabla_X)\nabla_X^{\mathrm{T}}\mathbf{Q}^{\mathrm{T}}+(\mu+\nu)\nabla_X^{\mathrm{T}}(N_i\nabla_X)\mathbf{I}+(\mu-\nu)\mathbf{Q}\nabla_X(N_i\nabla_X)^{\mathrm{T}}\mathbf{Q}^{\mathrm{T}}\big)\Delta\mathbf{u}\\&+\Big((\mu+\nu)\widehat{\mathbf{F}(N_i\nabla_X)}-(\mu-\nu)\mathbf{Q}\mathbf{F}^{\mathrm{T}}\widehat{\mathbf{Q}(N_i\nabla_X)}+2\lambda\mathbf{Q}(N_i\nabla_X)\boldsymbol{\ell}^{\mathrm{T}}\Big)\Delta\boldsymbol{\varphi},\end{aligned}\tag{42}$$

$$\begin{aligned}\Delta\mathbf{g}^{e2}_{\mathrm{M}_i}=&\Big(-(\mu+\nu)N_i\widehat{\mathbf{F}\nabla_X}+(\mu-\nu)N_i\widehat{\mathbf{Q}\nabla_X}\mathbf{F}\mathbf{Q}^{\mathrm{T}}+2\lambda N_i\boldsymbol{\ell}\nabla_X^{\mathrm{T}}\mathbf{Q}^{\mathrm{T}}\Big)\Delta\mathbf{u}\\&+\big(\alpha\mathbf{Q}(N_i\nabla_X)\nabla_X^{\mathrm{T}}\mathbf{Q}^{\mathrm{T}}+(\beta+\gamma)\nabla_X^{\mathrm{T}}(N_i\nabla_X)\mathbf{I}+(\beta-\gamma)\mathbf{Q}\nabla_X(N_i\nabla_X^{\mathrm{T}})\mathbf{Q}^{\mathrm{T}}\\&-(\mu+\nu)N_i\big(\mathbf{F}\mathbf{F}^{\mathrm{T}}-\mathrm{tr}(\mathbf{F}\mathbf{F}^{\mathrm{T}})\mathbf{I}\big)+(\mu-\nu)N_i\left[\mathbf{m_1}\ \mathbf{m_2}\ \mathbf{m_3}\right]+4\lambda N_i\boldsymbol{\ell}\boldsymbol{\ell}^{\mathrm{T}}\big)\Delta\boldsymbol{\varphi}.\end{aligned}\tag{43}$$

Now we substitute the Lagrangian interpolation of the kinematic field increments

$$\Delta\mathbf{u}^h=\sum_{j=1}^{n_{node}}N_j(\xi,\eta,\zeta)\Delta\mathbf{u}_j,\qquad\Delta\boldsymbol{\varphi}^h=\sum_{j=1}^{n_{node}}N_j(\xi,\eta,\zeta)\Delta\boldsymbol{\varphi}_j\tag{44}$$

in (39), (40), (42), (43) and by collecting the increments of nodal parameters in $\Delta\mathbf{d}^e_j=\begin{Bmatrix}\Delta\mathbf{u}_j\\\Delta\boldsymbol{\varphi}_j\end{Bmatrix}^e$ we obtain

$$\Delta\mathbf{g}^e_{\mathrm{G}_i}=\sum_{j=1}^{n_{node}}\mathbf{K}_{\mathrm{G}}{}^e_{ij}\Delta\mathbf{d}^e_j,\quad\Delta\mathbf{g}^e_{\mathrm{M}_i}=\sum_{j=1}^{n_{node}}\mathbf{K}_{\mathrm{M}}{}^e_{ij}\Delta\mathbf{d}^e_j.\tag{45}$$

We point out here that with $(44)_2$ we have opted for the Lagrangian interpolation of the so-called *spin variables*, which is just one of the possible interpolation options available. Such interpolation is known to suffer from both non-objectivity and path-dependence for low-order interpolation and coarse meshes [32], but it will be argued in the analysis of the numerical examples that much finer meshes are needed for a converged solution, thus making interpolation

$(44)_2$ completely acceptable. The 6×6 blocks of the element *geometric stiffness matrix* $\mathbf{K}_{\mathrm{G}}{}^{e}_{ij}$ now follow as

$$\mathbf{K}_{\mathrm{G}}{}^{e}_{ij} = \int_V \begin{bmatrix} \mathbf{0} & \mathbf{K}_{\mathrm{G}}{}^{e1}_{ij} \\ \mathbf{K}_{\mathrm{G}}{}^{e2}_{ij} & \mathbf{K}_{\mathrm{G}}{}^{e3}_{ij} \end{bmatrix} dV, \tag{46}$$

with the integrand submatrices equal to

$$\mathbf{K}_{\mathrm{G}}{}^{e1}_{ij} = -\widehat{\mathbf{Q}\mathbf{B}(N_i\nabla_X)}N_j, \tag{47}$$

$$\mathbf{K}_{\mathrm{G}}{}^{e2}_{ij} = N_i\widehat{\mathbf{Q}\mathbf{B}(N_j\nabla_X)}, \tag{48}$$

$$\mathbf{K}_{\mathrm{G}}{}^{e3}_{ij} = -\widehat{\mathbf{Q}\mathbf{G}(N_i\nabla_X)}N_j + N_iN_j\left[(\mathbf{F}\mathbf{B}^{\mathrm{T}}\mathbf{Q}^{\mathrm{T}})^{\mathrm{T}} - \mathrm{tr}(\mathbf{F}\mathbf{B}^{\mathrm{T}}\mathbf{Q}^{\mathrm{T}})\mathbf{I}\right]. \tag{49}$$

Likewise, the 6×6 blocks of the element *material stiffness matrix* $\mathbf{K}_{\mathrm{M}}{}^{e}_{ij}$ follow as

$$\mathbf{K}_{\mathrm{M}}{}^{e}_{ij} = \int_V \begin{bmatrix} \mathbf{K}_{\mathrm{M}}{}^{e1}_{ij} & \mathbf{K}_{\mathrm{M}}{}^{e2}_{ij} \\ \mathbf{K}_{\mathrm{M}}{}^{e3}_{ij} & \mathbf{K}_{\mathrm{M}}{}^{e4}_{ij} \end{bmatrix} dV, \tag{50}$$

where the integrand submatrices are

$$\begin{aligned} \mathbf{K}_{\mathrm{M}}{}^{e1}_{ij} &= \lambda\mathbf{Q}(N_i\nabla_X)(N_j\nabla_X)^{\mathrm{T}}\mathbf{Q}^{\mathrm{T}} + (\mu+\nu)(N_j\nabla_X)^{\mathrm{T}}(N_i\nabla_X)\mathbf{I} \\ &\quad + (\mu-\nu)\mathbf{Q}(N_j\nabla_X)(N_i\nabla_X)^{\mathrm{T}}\mathbf{Q}^{\mathrm{T}}, \end{aligned} \tag{51}$$

$$\mathbf{K}_{\mathrm{M}}{}^{e2}_{ij} = (\mu+\nu)\widehat{\mathbf{F}(N_i\nabla_X)}N_j - (\mu-\nu)\mathbf{Q}\mathbf{F}^{\mathrm{T}}\widehat{\mathbf{Q}(N_i\nabla_X)}N_j + 2\lambda\mathbf{Q}(N_i\nabla_X)\boldsymbol{\ell}^{\mathrm{T}}N_j, \tag{52}$$

$$\mathbf{K}_{\mathrm{M}}{}^{e3}_{ij} = -(\mu{+}\nu)N_i\widehat{\mathbf{F}(N_j\nabla_X)} + (\mu{-}\nu)N_i\widehat{\mathbf{Q}(N_j\nabla_X)}\mathbf{F}\mathbf{Q}^{\mathrm{T}} + 2\lambda N_i\boldsymbol{\ell}(N_j\nabla_X)^{\mathrm{T}}\mathbf{Q}^{\mathrm{T}}, \tag{53}$$

$$\begin{aligned} \mathbf{K}_{\mathrm{M}}{}^{e4}_{ij} &= \alpha\mathbf{Q}(N_i\nabla_X)(N_j\nabla_X^{\mathrm{T}})\mathbf{Q}^{\mathrm{T}} + (\beta+\gamma)(N_j\nabla_X^{\mathrm{T}})(N_i\nabla_X)\mathbf{I} \\ &\quad + (\beta-\gamma)\mathbf{Q}(N_j\nabla_X)(N_i\nabla_X^{\mathrm{T}})\mathbf{Q}^{\mathrm{T}} - (\mu+\nu)N_iN_j\left(\mathbf{F}\mathbf{F}^{\mathrm{T}} - \mathrm{tr}(\mathbf{F}\mathbf{F}^{\mathrm{T}})\mathbf{I}\right) \\ &\quad + (\mu-\nu)N_iN_j\left[\mathbf{m_1}\ \mathbf{m_2}\ \mathbf{m_3}\right] + 4\lambda N_iN_j\boldsymbol{\ell}\boldsymbol{\ell}^{\mathrm{T}}. \end{aligned} \tag{54}$$

Finally, the element tangent stiffness matrix follows as the sum of the geometric and material stiffness block matrices (46) and (50) as

$$\mathbf{K}^e = \begin{bmatrix} \mathbf{K}_{\mathrm{M}11}^{e} + \mathbf{K}_{\mathrm{G}11}^{e} & \mathbf{K}_{\mathrm{M}12}^{e} + \mathbf{K}_{\mathrm{G}12}^{e} & \cdots & \mathbf{K}_{\mathrm{M}1n}^{e} + \mathbf{K}_{\mathrm{G}1n}^{e} \\ \mathbf{K}_{\mathrm{M}21}^{e} + \mathbf{K}_{\mathrm{G}21}^{e} & \mathbf{K}_{\mathrm{M}22}^{e} + \mathbf{K}_{\mathrm{G}22}^{e} & \cdots & \mathbf{K}_{\mathrm{M}2n}^{e} + \mathbf{K}_{\mathrm{G}2n}^{e} \\ \vdots & \vdots & \ddots & \vdots \\ \mathbf{K}_{\mathrm{M}n1}^{e} + \mathbf{K}_{\mathrm{G}n1}^{e} & \mathbf{K}_{\mathrm{M}n2}^{e} + \mathbf{K}_{\mathrm{G}n2}^{e} & \cdots & \mathbf{K}_{\mathrm{M}nn}^{e} + \mathbf{K}_{\mathrm{G}nn}^{e} \end{bmatrix}, \tag{55}$$

which serves to express linear increment in the element residual (29) as

$$\Delta \mathbf{g}^e = \mathbf{K}^e \Delta \mathbf{d}^e \quad \text{where} \ \ \Delta \mathbf{d}^{e^{\mathrm{T}}} = \langle \Delta \mathbf{d}_1^{e^{\mathrm{T}}} \ \Delta \mathbf{d}_2^{e^{\mathrm{T}}} \ \ldots \Delta \mathbf{d}_n^{e^{\mathrm{T}}} \rangle \ \ \text{with} \ \ \Delta \mathbf{d}_i^e = \begin{Bmatrix} \Delta \mathbf{u}_i \\ \Delta \boldsymbol{\varphi}_i \end{Bmatrix}^e \tag{56}$$

and n representing the number of nodes on the element (for clarity here introduced instead of n_{node}).

From this point on, we can proceed towards the standard finite element assembly accounting for all element contributions, i.e.

$$\mathbf{K} = \overset{n_{elem}}{\underset{e=1}{\mathbb{A}}} \mathbf{K}^e, \quad \mathbf{q}^{int} = \overset{n_{elem}}{\underset{e=1}{\mathbb{A}}} \mathbf{q}^{int,e}, \quad \mathbf{q}^{ext} = \overset{n_{elem}}{\underset{e=1}{\mathbb{A}}} \mathbf{q}^{ext,e}. \tag{57}$$

After additionally introducing the boundary conditions we obtain the global system of equations we need to solve as

$$\Delta \mathbf{d} = -\mathbf{K}^{-1} \left(\mathbf{q}^{int} - \mathbf{q}^{ext} \right), \tag{58}$$

where $\Delta \mathbf{d} = \overset{n_{elem}}{\underset{e=1}{\mathbb{A}}} \Delta \mathbf{d}^e$ represents the global vector of nodal incremental displacements and incremental microrotations, which are the basic unknowns of our problem, $\mathbf{K}$ is the global stiffness matrix, $\mathbf{q}^{int}$ is the global internal force vector and $\mathbf{q}^{ext}$ is the global external force vector.

In the predictor part of the non-linear Newton–Raphson solution procedure, the geometric stiffness vanishes and the element stiffness matrix (55) coinicides with the stiffness matrix in the linear finite elements with Lagrangian interpolation. The lowest-order member of the family of Lagrangian elements was successfully patch-tested for convergence in [13].

4.2. Iterative update procedure

Once $\Delta\mathbf{d}$ has been obtained from (58), it is used to provide the updated values for $\mathbf{q}^{int}$ and $\mathbf{K}$ so that the procedure may be repeated until a satisfactorily accurate solution has been achieved (e.g. through a sufficiently small residual, displacement and/or energy norm). To update $\mathbf{q}^{int}$ and $\mathbf{K}$ we consider their nodal expressions at an element level $\mathbf{q}_i^{int,e}$ in (24) and $\mathbf{K}_{ij}^e = \mathbf{K}_{\mathrm{G}}{}_{ij}^{e} + \mathbf{K}_{\mathrm{M}}{}_{ij}^{e}$ defined in (46) and (50), showing that at each integration point we need the updated kinematics ($\mathbf{F} = \mathrm{GRAD}\mathbf{x},\ \mathbf{Q}$) and the updated stress and couple-stress tensors ($\mathbf{B} = \boldsymbol{\mathcal{T}} : \mathbf{E},\ \mathbf{G} = \boldsymbol{\mathcal{D}} : \mathbf{K}$). For the former, we need to outline the procedure to obtain the updated position vector $\mathbf{x}$ and orientation tensor $\mathbf{Q}$ at the integration-point level, while for the latter we need to do the same for the micropolar strain and curvature tensors $\mathbf{E}$ and $\mathbf{K}$. This is shown next.

4.2.1. Update of position and orientation

To update the position vector at each integration point it is sufficient to extract $\Delta\mathbf{u}_i^e$ from $\Delta\mathbf{d} = \overset{n_{elem}}{\underset{e=1}{\mathbb{A}}} \Delta\mathbf{d}^e$ and (56) to obtain the corresponding nodal displacement at iteration $k+1$ as

$$\mathbf{u}_i^{(k+1)^e} = \mathbf{u}_i^{(k)^e} + \Delta\mathbf{u}_i^e, \tag{59}$$

from where the integration-point value is obtained from $(44)_1$ and the corresponding position from $\mathbf{x} = \mathbf{X} + \mathbf{u}$ as per Figure 1.

To update the orientation tensor at each integration point we need to respect the non-linearity of the 3D-rotation space whereby a new orientation $\mathbf{Q}_2$ is obtained from an existing one $\mathbf{Q}_1$ as

$$\mathbf{Q}_2 = \exp\widehat{\boldsymbol{\vartheta}}\mathbf{Q}_1, \tag{60}$$

with $\boldsymbol{\vartheta}$ as the rotation vector transforming $\mathbf{Q}_1$ into $\mathbf{Q}_2$ and $\exp\widehat{\boldsymbol{\vartheta}}$ having a closed-form expression (see e.g. [33] for a simple derivation of this result):

$$\exp\widehat{\boldsymbol{\vartheta}} = \mathbf{I} + \frac{\sin\vartheta}{\vartheta}\hat{\boldsymbol{\vartheta}} + \frac{1-\cos\vartheta}{\vartheta^2}\hat{\boldsymbol{\vartheta}}^2 \tag{61}$$

where $\vartheta = ||\boldsymbol{\vartheta}||$. More on parametrisation of 3D rotations may be found e.g. in [34, 35, 36, 37]. In the current procedure with interpolation of the microrotational spins $(44)_2$, this would normally mean: (i) storing the existing orientation tensors $\mathbf{Q}^{(k)}$ in each element integration point, (ii) obtaining the integration-point value of $\Delta\boldsymbol{\varphi}^h$ from $(44)_2$ with $\Delta\boldsymbol{\varphi}_i^e$ taken from $\Delta\mathbf{d}$ and (56) and (iii) performing the integration-point update as

$$\mathbf{Q}^{(k+1)} = \exp\widehat{\Delta\boldsymbol{\varphi}^h}\mathbf{Q}^{(k)}. \tag{62}$$

In the actual algorithm coded, the integration-point matrices are expressed via the so-called quaternion parametrisation (see e.g. [35, 37]), which has shown to be in favour of the computational cost saving. In general, after obtaining the vector increment of the microrotation field $\Delta\boldsymbol{\varphi}^{(k)}$ in the k-th iteration we form the corresponding quaternion increment as

$$\boldsymbol{q'}^{(k)}_{\Delta\boldsymbol{\varphi}} = \left\{q^{(k)}_{\Delta\varphi},\ \boldsymbol{q}^{(k)}_{\Delta\boldsymbol{\varphi}}\right\} = \left\{\cos\left(\frac{\Delta\varphi^{(k)}}{2}\right),\ \frac{\sin\left(\frac{\Delta\varphi^{(k)}}{2}\right)}{\Delta\varphi^{(k)}}\Delta\boldsymbol{\varphi}^{(k)}\right\}, \tag{63}$$

where $\Delta\varphi^{(k)} = ||\Delta\boldsymbol{\varphi}^{(k)}||$. The quaternion update is defined through the quaternion multiplication (the quaternion counterpart of (62)), i.e.

$$\boldsymbol{q'}^{(k+1)} = \boldsymbol{q'}^{(k)}_{\Delta\boldsymbol{\varphi}} \circ \boldsymbol{q'}^{(k)} = \left\{q_0^{(k+1)},\ \boldsymbol{q}^{(k+1)}\right\}, \tag{64}$$

where $\boldsymbol{q'}^{(k)} = \left\{q_0^{(k)},\ \boldsymbol{q}^{(k)}\right\}$ is the quaternion obtained in the previous (k^{th}) iteration. The updated quaternion is obtained as [36]

$$\boldsymbol{q'}^{(k+1)} = \left\{ q_{\Delta\varphi}^{(k)} \cdot q_0^{(k)} - \boldsymbol{q}_{\Delta\boldsymbol{\varphi}}^{(k)} \cdot \boldsymbol{q}^{(k)},\ \boldsymbol{q}_{\Delta\boldsymbol{\varphi}}^{(k)} \times \boldsymbol{q}^{(k)} + q_0^{(k)} \cdot \boldsymbol{q}_{\Delta\boldsymbol{\varphi}}^{(k)} + q_{\Delta\varphi}^{(k)} \cdot \boldsymbol{q}^{(k)} \right\}, \tag{65}$$

from where the updated orientation matrix $\mathbf{Q}^{(k+1)}$ follows as

$$\mathbf{Q}^{(k+1)} = (2q_0^{(k+1)^2} - 1)\mathbf{I} + 2q_0^{(k+1)}\widehat{\boldsymbol{q}^{(k+1)}} + 2\boldsymbol{q}^{(k+1)} \otimes \boldsymbol{q}^{(k+1)}. \tag{66}$$

4.2.2. Update of strain, curvature, stress and couple-stress tensors

In order to update the Biot-like strain and curvature tensors $\mathbf{E}$ and $\mathbf{K}$ we need to know the values of the displacement field and orientation matrix at the integration points, which we now do. The components of the deformation gradient $\mathbf{F}$ are easily obtained by differentiating the interpolated displacement values at the integration point l as follows:

$$\mathbf{F} = \mathrm{GRAD}\mathbf{x} = \mathbf{I} + \mathrm{GRAD}\left(\sum_{j=1}^{n_{node}} N_i \mathbf{u}_i\right)\Bigg|_{(\xi_l,\eta_l,\zeta_l)} \tag{67}$$

$$= \mathbf{I} + \sum_{j=1}^{n_{node}} \begin{Bmatrix} u_{i1} \\ u_{i2} \\ u_{i3} \end{Bmatrix} \otimes \begin{Bmatrix} \frac{\partial N_i}{\partial X_1} \\ \frac{\partial N_i}{\partial X_2} \\ \frac{\partial N_i}{\partial X_3} \end{Bmatrix}\Bigg|_{(\xi_l,\eta_l,\zeta_l)} \tag{68}$$

and the values of the orientation matrix are obtained as explained in Section 4.2.1. Then, the current strain tensor is evaluated by substituting the obtained matrices $\mathbf{F}$ and $\mathbf{Q}$ into equation (9).

In order to update the curvature tensor, we start by extracting the curvature vector $\mathbf{K}_i$ from $\mathbf{K} = \mathbf{K}_i \otimes \mathbf{E}_i$. The curvature vector $\mathbf{K}_i$ is defined in Section 2.2 as

$$\mathbf{K}_i = \mathrm{ax}\left(\mathbf{Q}^{\mathrm{T}}\frac{\partial \mathbf{Q}}{\partial X_i}\right). \tag{69}$$

Next, we introduce $\mathbf{Q} = \exp(\widehat{\Delta\boldsymbol{\varphi}})\mathbf{Q}_{\mathrm{old}}$ (where $\mathbf{Q}_{\mathrm{old}}$ and $\mathbf{Q}$ are the orientations in the previous and the current iteration) into $\widehat{\mathbf{K}_i} = \mathbf{Q}^{\mathrm{T}}\dfrac{\partial \mathbf{Q}}{\partial X_i}$ and obtain

$$
\begin{aligned}
\widehat{\mathbf{K}_i} &= \mathbf{Q}_{\mathrm{old}}^{\mathrm{T}}\exp(\widehat{\Delta\boldsymbol{\varphi}})^{\mathrm{T}}\frac{\partial\left(\exp(\widehat{\Delta\boldsymbol{\varphi}})\mathbf{Q}_{\mathrm{old}}\right)}{\partial X_i} \\
&= \mathbf{Q}_{\mathrm{old}}^{\mathrm{T}}\exp(\widehat{\Delta\boldsymbol{\varphi}})^{\mathrm{T}}\frac{\partial\exp(\widehat{\Delta\boldsymbol{\varphi}})}{\partial X_i}\mathbf{Q}_{\mathrm{old}} + \mathbf{Q}_{\mathrm{old}}^{\mathrm{T}}\underbrace{\exp(\widehat{\Delta\boldsymbol{\varphi}})^{\mathrm{T}}\exp(\widehat{\Delta\boldsymbol{\varphi}})}_{\mathbf{I}}\frac{\partial\mathbf{Q}_{\mathrm{old}}}{\partial X_i} \\
&= \mathbf{Q}_{\mathrm{old}}^{\mathrm{T}}\exp(\widehat{\Delta\boldsymbol{\varphi}})^{\mathrm{T}}\frac{\partial\exp(\widehat{\Delta\boldsymbol{\varphi}})}{\partial X_i}\mathbf{Q}_{\mathrm{old}} + \widehat{\mathbf{K}}_{i\mathrm{old}}.
\end{aligned}
$$

Next, we rewrite $\mathbf{Q}_{\mathrm{old}}$ as $\mathbf{Q}_{\mathrm{old}} = \exp(\widehat{\Delta\boldsymbol{\varphi}})^{\mathrm{T}}\mathbf{Q}$ and obtain

$$
\widehat{\mathbf{K}_i} = \mathbf{Q}^{\mathrm{T}}\frac{\partial\exp(\widehat{\Delta\boldsymbol{\varphi}})}{\partial X_i}\exp(\widehat{\Delta\boldsymbol{\varphi}})^{\mathrm{T}}\mathbf{Q} + \widehat{\mathbf{K}}_{i\mathrm{old}}. \tag{70}
$$

297 After a lengthy, but otherwise straightforward algebraic manipulation of the
298 term $\dfrac{\partial\exp(\widehat{\Delta\boldsymbol{\varphi}})}{\partial X_i}\exp(\widehat{\Delta\boldsymbol{\varphi}})^{\mathrm{T}}$ (which is presented in detail e.g. in [38]) we obtain

$$
\widehat{\mathbf{K}_i} = \widehat{\mathbf{Q}^{\mathrm{T}}\mathbf{H}(\Delta\boldsymbol{\varphi})\frac{\partial\Delta\boldsymbol{\varphi}}{\partial X_i}} + \widehat{\mathbf{K}}_{i\mathrm{old}} \quad\Leftrightarrow\quad \mathbf{K}_i = \mathbf{K}_{i_{\mathrm{old}}} + \mathbf{Q}^{\mathrm{T}}\mathbf{H}(\Delta\boldsymbol{\varphi})\frac{\partial\Delta\boldsymbol{\varphi}}{\partial X_i}, \tag{71}
$$

299 where

$$
\mathbf{H}(\Delta\boldsymbol{\varphi}) = \mathbf{I} + \frac{1-\cos(\Delta\varphi)}{(\Delta\varphi)^2}\widehat{\Delta\boldsymbol{\varphi}} + \frac{\Delta\varphi - \sin(\Delta\varphi)}{(\Delta\varphi)^3}\widehat{\Delta\boldsymbol{\varphi}}^2, \tag{72}
$$

300 is the tangent map transforming the linear change of a rotation vector into a
301 rotational spin (see e.g. [25]) and $\Delta\varphi = ||\Delta\boldsymbol{\varphi}||$. Finally, the updated curvature
302 tensor is composed from the three updated curvature vectors $\mathbf{K}_i$ $(i = 1, 2, 3)$ as
303 $\mathbf{K} = \mathbf{K}_i \otimes \mathbf{E}_i$ (see Section 2.2), which can be written as

$$
\mathbf{K} = \mathbf{K}_{\mathrm{old}} + \mathbf{Q}^{\mathrm{T}}\mathbf{H}(\Delta\boldsymbol{\varphi})\mathrm{GRAD}(\Delta\boldsymbol{\varphi}). \tag{73}
$$

304 With the strain and curvature tensors thus obtained we can easily update our
305 stress and couple-stress tensors from (11) and (13).

306 Both finite elements Hex8NL and Hex27NL are implemented using full Gauss
307 quadrature integration scheme (8-point integration for Hex8NL, 27-point inte-

gration for Hex27NL) applied to (23)-(25), (46) and (50). The reduced integration scheme (1-point integration for Hex8NL, 8-point integration for Hex27NL) is also tested and leads to a loss of convergence.

5. Numerical examples

The presented finite elements are implemented within the finite element analysis program FEAP [39] and tested against three representative non-linear numerical examples: *(i)* pure bending of a straight beam, *(ii)* combined bending and torsion of a T-shaped structure and *(iii)* deformation of a curved cantilever subject to out-of-plane force at the free end. The first example's solution is tested against a non-linear generalisation of the linear analytical solution [40] derived in this work. It is reasonable to assume that such generalisation is applicable to thin specimens. The solution of the second example is compared to the results of [19], where this problem was proposed and numerically analysed in non-linear micropolar elasticity for the first time. Finally, we take the well-known 45°-bend test [41], often analysed in various beam formulations (e.g. [42], [32]), as an example exhibiting a genuine 3D large-deformation behaviour and analyse the influence of micropolar effects in the results obtained. All the presented numerical results are computed using the energy-convergence criterion $\Delta\mathbf{d}^{\mathrm{T}}(\mathbf{q}^{int} - \mathbf{q}^{ext}) \leq 10^{-16}$.

5.1. Pure bending of a cantilever

The pure bending state of a beam is a state in which a resultant bending moment applied to the beam does not produce any cross-sectional stress resultants and the axis of the beam is bent into a circular curve. Consequently, throughout deformation, the beam cross-sections remain planar and perpendicular to the axis of the beam. For a cantilever, the problem is presented in Figure 4 where the boundary conditions are applied as follows: (i) the displacements along the axes x and z and all the microrotation components in the plane $x = 0$ are equal to zero, (ii) the displacements along the axis y at $x = 0$ and $y = 0$ are equal to zero, (iii) the displacements along the axis z on the planes $z = \mp\frac{b}{2}$ are equal to zero, (iv) the microrotations around the axes x and y on the planes $z = \mp\frac{b}{2}$ are equal to zero, and (v) a resultant bending moment is applied on the cross-section at $x = L$. In order to generalise the plane-strain linear micropolar solution of Gauthier and Jahsman [40] (in which the resultant bending moment at the free end is given in terms of the distributed loadings p_0 and m_{sz} in Figure 4) to the non-linear case, we consider the situation in which the solution is also valid in plane stress (i.e. for $n = 0$), hence the boundary conditions as defined. Then, a non-linear micropolar solution is induced from the known Euler elastica result, which is expected to remain valid for relatively thin specimens.

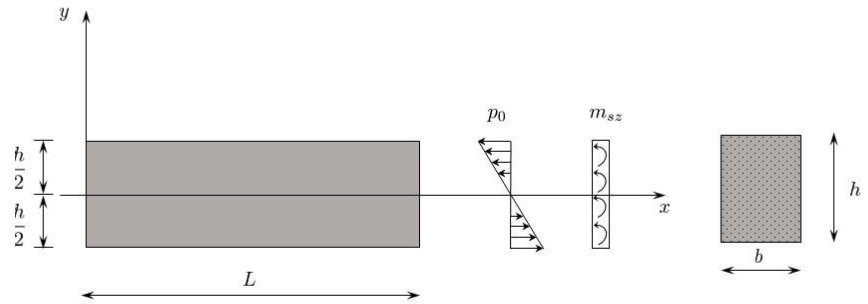

Figure 4: Pure bending of a cantilever beam

5.1.1. *Linear micropolar analytical solution (Gauthier and Jahsman [40]) for* $n = 0$

Gauthier and Jahsman have shown that in the micropolar continuum the state of pure bending requires that the resultant bending moment is applied via *both* a linearly varying normal surface traction p_0 *and* a constant surface moment m_{sz} (see Figure 4)) , i.e. $M_z = b\int_{-\frac{h}{2}}^{\frac{h}{2}}(y\, p_{sx} + m_{sz})dy$. In order to produce pure bending in fact they have to be applied in *a unique proportion* equal to $\dfrac{m_{sz}}{p_0} = \dfrac{4l_b^2}{h}$ for the presently considered case with no Poisson effect ($n = 0$). Obviously, for a material with vanishing characteristic length ($l_b \to 0$) the state of pure bending may not be achieved if the surface moment loading is present, while for a general micropolar material such a state is only possible when m_{sz} and p_0 are given in the proportion defined above resulting in $M = p_0 W_z + m_{sz} A$ with $A = bh$ and $W_z = bh^2/6$. As a result,

$$p_0 = -\frac{1}{1+\delta}\frac{M_z}{W_z}, \quad m_{sz} = \frac{\delta}{1+\delta}\frac{M_z}{A}, \tag{74}$$

with $\delta = 24\left(\frac{l_b}{h}\right)^2$, while the only non-vanishing stress components are

$$\sigma_{xx} = -\frac{1}{1+\delta}\frac{M_z y}{I_z}, \quad \mu_{zx} = \frac{\delta}{1+\delta}\frac{M_z}{A}, \tag{75}$$

with $I_z = \frac{bh^3}{12}$ and the displacement and rotation fields are

$$\varphi = \frac{1}{1+\delta}\frac{M_z x}{I_z}, \quad u = -\frac{1}{1+\delta}\frac{M_z xy}{I_z}, \quad v = \frac{1}{1+\delta}\frac{M_z x^2}{2I_z}. \tag{76}$$

This problem does not induce any non-symmetry in the stress tensor field, i.e. the solution does not depend on the coupling number N (and therefore also on the material parameter ν). For $l_b \to 0$, the classical solution is approached in all fields.

5.1.2. Non-linear beam solution

This solution follows from the equilibrium

$$\frac{d\varphi_z(x,0,z)}{dx} = \frac{M_z}{EI_z}, \tag{77}$$

which shows that the beam reference axis turns into a circular arc of curvature $\frac{M_z}{EI_z}$ with $\varphi_z(x,0,z) = \frac{M_z x}{EI_z}$, $u(x,0,z) = -x + \frac{EI_z}{M_z}\sin\varphi_z(x,0,z)$, $v(x,0,z) = \frac{EI_z}{M_z}(1-\cos\varphi_z(x,0,z))$. Since in the beam theory the cross-sections remain rigid and for the present pure-bending state they also remain orthogonal to the deformed beam axis, we thus obtain

$$\varphi_z = \frac{M_z x}{EI_z}, \tag{78}$$

$$u = u(x,0,z) - y\sin\varphi_z = \left(\frac{EI_z}{M_z} - y\right)\sin\frac{M_z x}{EI_z} - x, \tag{79}$$

$$v = v(x,0,z) - y\left(1-\cos\varphi_z\right) = \left(\frac{EI_z}{M_z} - y\right)\left(1 - \cos\frac{M_z x}{EI_z}\right). \tag{80}$$

In the linear analysis, the solution is obtained as the lowest-order expansion of the above results and gives

$$\varphi_z = \frac{M_z x}{EI_z}, \quad u = -\frac{M_z x y}{EI_z} \quad \text{and} \quad v = \frac{M_z x^2}{2EI_z}, \tag{81}$$

which turns out to be precisely the special case of the linear micropolar solution for $n = 0$ (76) when there are no micropolar effects present ($\delta = 0$).

This inspires us to assume that in the micropolar pure bending the bending stiffness should increase by the factor $1+\delta$ also in non-linear analysis thus leading to:

$$\varphi_z = \frac{1}{1+\delta}\frac{M_z x}{EI_z}, \tag{82}$$

$$u = \left((1+\delta)\frac{EI_z}{M_z} - y\right)\sin\frac{M_z x}{(1+\delta)EI_z} - x, \tag{83}$$

$$v = \left((1+\delta)\frac{EI_z}{M_z} - y\right)\left(1 - \cos\frac{M_z x}{(1+\delta)EI_z}\right). \tag{84}$$

This assumption makes sense for thin specimens ($\frac{h}{L} << 1$), in which the through-the-thickness normal stresses cannot significantly develop. In (82)-(84), $M_z = p_0 W_z + m_{sz} A$ is the resultant bending moment in which now it has to be recognised that the applied load traction p_0 has to stay orthogonal to the cross-section at all times. The load traction p_0 thus ought to point in the direction of $\mathbf{t}_{1L} = \mathbf{Q}_L \mathbf{e_1}$, with $\mathbf{Q}_L$ as the rotation matrix of the cross-section at $x = L$. Therefore, we now have $p_x = -p_0 \frac{2y}{h}\cos\varphi_{zL}$ and $p_y = -p_0\frac{2y}{h}\sin\varphi_{zL}$ with $\varphi_{zL} = \frac{1}{1+\delta}\frac{M_z L}{EI_z}$. Such loading, which follows the structure as it deforms, is called *follower* loading.

5.1.3. Follower loading in the non-linear finite-element solution process

By introducing the follower loads (i.e. keeping the nodal forces orthogonal to the cantilever cross-section during the whole deformation process), the external loading ceases to be constant, since it becomes dependent on the orientation matrix $\mathbf{Q}$ (see [43] for more detail on follower loading). Consequently, when linearizing the residual $\mathbf{g}^e = \mathbf{q}^{int,e} - \mathbf{q}^{ext,e}$, the non-constant external loading also contributes to the element stiffness matrix $\mathbf{K}^e$ in equation (55). For a loaded node N the contribution of the follower external force vector thus becomes

$$\mathbf{K}^e_{\mathrm{EXT}ij} = \delta_{iN}\delta_{jN} \begin{bmatrix} \mathbf{0} & \widehat{\mathbf{Q}_N \widetilde{\mathbf{F}}_N} \\ \mathbf{0} & \mathbf{0} \end{bmatrix}, \tag{85}$$

where $\mathbf{Q}_N$ represent the nodal orientation matrix at node N and $\widetilde{\mathbf{F}}_N$ the nodal follower-force vector. The summation convention does not apply to N, but contribution (85) has to be computed for each node subject to a follower force. The ij block of the element stiffness matrix $\mathbf{K}^e$ is then computed as $\left[\mathbf{K}^e_{ij}\right] = \left[\mathbf{K}_{\mathrm{M}}{}^e_{ij}\right] + \left[\mathbf{K}_{\mathrm{G}}{}^e_{ij}\right] + \left[\mathbf{K}^e_{\mathrm{EXT}ij}\right]$. It is very important to take this into account in order to provide consistent linearisation of the residual vector and thus keep the quadratic convergence rate during the Newton–Raphson solution procedure.

5.1.4. Numerical solution

We now model a thin cantilever beam subject to pure bending as shown in Figure 5 using our elements Hex8NL and Hex27NL and observe its non-linear behavior. The chosen geometry of the cantilever is $L = 10$ m, $h = 0.1$ m and $b = 1$ m, and, in order to capture the size-effect the value of the characteristic length is varied in the region $l_b \in [0.01, 0.08]$ m (10-80% of the specimen's thickness). The rotations around x and y as well as the displacements along z are restrained at all the nodes in the mesh used, while the rotations along z and the displacements along x are also restrained at the cross-section with $x = 0$, and the displacements along y are also restrained along the edge with $x = 0$ and

$y = 0$. The resultant bending moment $M_z = 0.01\pi$ Nm is applied through a linearly varying surface force $P_{S1} = \left(1 - \frac{2y}{h}\right) p_0$ and a constant surface moment loading $M_{S3} = m_{sz}$. As explained in Sections 5.1.1 - 5.1.3, the applied loadings have to be prescribed in the defined ratio $\dfrac{m_{sz}}{p_0} = \dfrac{4l_b^2}{h}$, while the surface force P_{S1} has to be applied as a follower load, i.e. it has to remain orthogonal to the cantilever cross-section at the free end during the whole deformation process. The analytical values of the loading magnitudes p_0 and m_{sz} for given M_z and different l_b are presented in Table 1. The distributed loadings P_{S1} and M_{S3} are applied through corresponding concentrated nodal forces and moments obtained by integration.

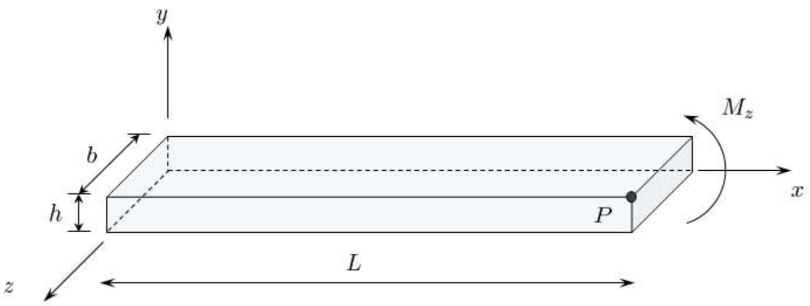

Figure 5: Thin cantilever beam subject to bending

The engineering material parameters are taken as $E = 1200$ N/m^2 and $n = 0.0$ which give the Lamé constants $\mu = 600$ N/m^2 and $\lambda = 0$ N/m^2. The parameter ν is chosen as $\nu = 200$ N/m^2 (equivalent to $N = 0.5$). The remaining engineering parameters which exist only in the 3D analysis are chosen as $\psi = 1$ and $l_t = 0.02$ m, but, since they do not affect the solution, they can have arbitrary values.

Table 1: External loadings p_0 and m_{sz} for different values of the characteristic length l_b and $h = 0.1$, giving the total external moment $M = 0.01\pi$ Nm

l_b/h	l_b	$\beta + \gamma$	p_0	m_{sz}
0.1	0.01	0.24	15.201 254 775 434 490	0.060 805 019 101 737 940
0.2	0.02	0.96	9.617 120 368 132 020	0.153 873 925 890 112 300
0.4	0.04	3.84	3.894 536 347 425 364	0.249 250 326 235 223 300
0.8	0.08	15.36	1.152 173 344 837 332	0.294 956 376 278 357 100

First, the problem is solved using a mesh of 64 hexahedral finite elements Hex8NL and Hex27NL propagating in the x direction. The numerical results for the horizontal and vertical displacements u_1 and u_2 and microrotation φ_3 at node $P(L, h, b)$ in Figure 5 are compared against the analytical solution derived in Section 5.1. The results obtained using the Hex8NL element are shown in Table 2 and Figure 6, while the results obtained using the Hex27NL element are shown only graphically in Figure 6.

Table 2: Displacement components of node $P(L, h, b)$ obtained using $64 \times 1 \times 1$ Hex8NL elements, A = Analytical, N = Numerical, LS = Number of load steps, niter = number of iterations

l_b	LS	A u_1	N u_1	A u_2	N u_2	A φ_3	N φ_3	niter	CPU time
0.01	1	-7.774	-1.927	7.096	4.923	2.534	1.094	18	2 sec
0.02	1	-3.814	-1.268	6.387	4.088	1.603	0.876	14	1.5 sec
0.04	1	-0.718	-0.412	3.123	2.376	0.650	0.486	11	1 sec
0.08	1	-0.071	-0.059	0.956	0.870	0.192	0.175	5	0.5 sec

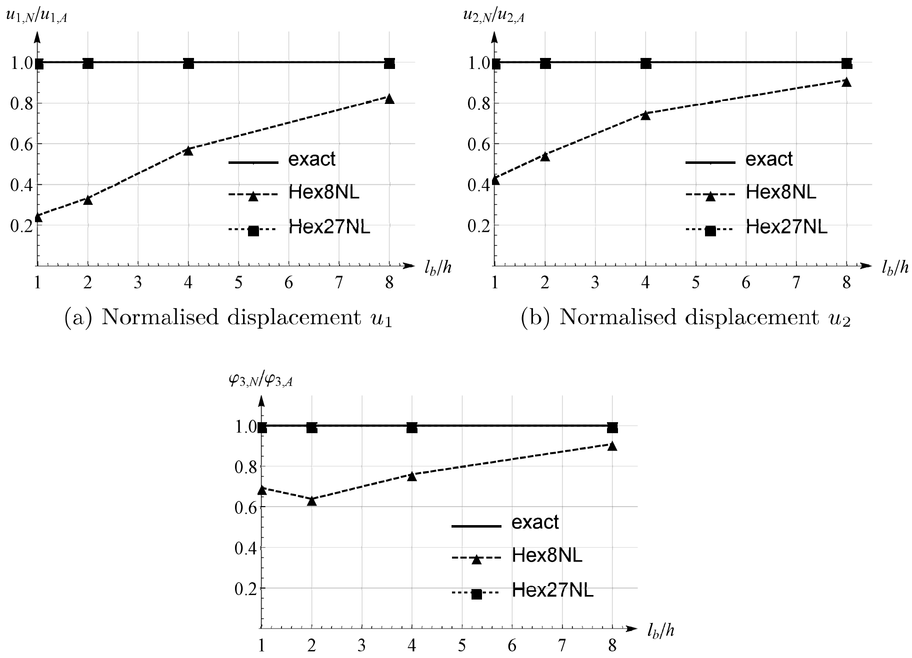

(a) Normalised displacement u_1

(b) Normalised displacement u_2

(c) Normalised microrotation φ_3

Figure 6: Cantilever beam subject to pure bending - displacements at node $P(L, h, b)$ for Hex8NL and Hex27NL using a 64 element mesh

By increasing the value of the characteristic length, the cantilever becomes stiffer (also observed in the linear analysis; see [13]). Hex8NL shows quite poor results, especially for small micropolar effects, a phenomenon also observed in the linear analysis, while Hex27NL shows results which correspond closely with the derived analytical results for the whole range of l_b. For the Hex8NL element, the finite element mesh is further refined to 2048 elements and the obtained results are presented in Table 3. The analytical result is now approached in all the observed results, and the accuracy is achieved in three significant digits. The deformed configuration for the softest configuration ($l_b = 0.01$) in the last (fifth) load step obtained by 64 Hex27NL finite element is shown in Figure 7. We conclude that the newly presented finite elements converge to the analytical result assumed to hold, which makes this example a possible benchmark problem for testing the validity of new geometrically non-linear micropolar finite elements.

Table 3: Displacement components of node $P(L, h, b)$ obtained using $2048 \times 1 \times 1$ Hex8NL element, A = Analytical, N = Numerical, LS = Number of load steps, niter = number of iterations

l_b	LS	A	N	A	N	A	N	niter	CPU
		u_1	u_1	u_2	u_2	φ_3	φ_3		time
0.01	5	-7.774	-7.776	7.096	7.097	2.534	2.530	5*11	524 min 44 sec
0.02	5	-3.814	-3.809	6.387	6.385	1.603	1.602	5*9	428 min 34 sec
0.04	1	-0.718	-0.717	3.121	3.121	0.650	0.649	11	103 min 45 sec
0.08	1	-0.071	-0.071	0.956	0.956	0.192	0.192	5	45 min 08 sec

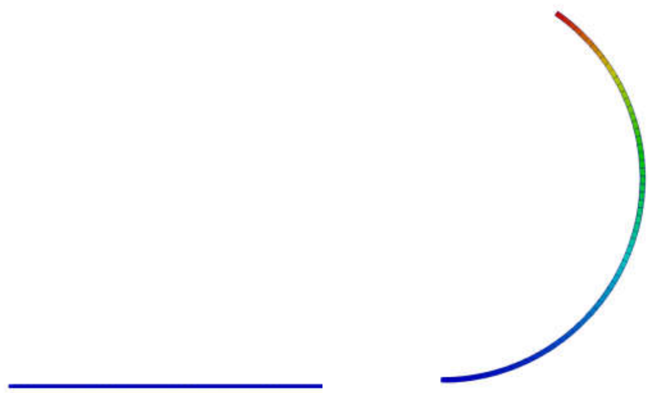

(a) No loading (b) Load step 5

Figure 7: Undeformed and deformed configuration of the cantilever beam for $l_b = 0.01$ using a mesh of $64 \times 1 \times 1$ Hex27NL elements

In order to demonstrate the *importance of consistent linearisation* in problems with follower forces, the problem is solved using 64 Hex27NL finite elements for $l_b = 0.02$ also without $\mathbf{K}^e_{\mathrm{EXT}ij}$. The convergence rate with and without $\mathbf{K}^e_{\mathrm{EXT}ij}$ is given in Table 4. We can see that *without consistent linearisation* of the residual, *the number of iterations increases from 14 to 19* and *the quadratic convergence rate of the Newton–Raphson method is lost.* However, in both cases we converge to the same solution, as expected.

Table 4: Convergence rate of the Newton–Raphson scheme using 64 Hex27NL elements for $l_b = 0.02$ and load increment 1 ; residual and energy norms

	with $\mathbf{K}^{e}_{\mathrm{EXT}ij}$		without $\mathbf{K}^{e}_{\mathrm{EXT}ij}$	
It	Residual norm	Energy norm	Residual norm	Energy norm
0	$8.02{\cdot}10^{-2}$	$1.25{\cdot}10^{-2}$	$8.02{\cdot}10^{-2}$	$1.25{\cdot}10^{-2}$
1	$1.45{\cdot}10^{\ 2}$	$4.37{\cdot}10^{\ 1}$	$1.45{\cdot}10^{2}$	$4.37{\cdot}10^{1}$
$\vdots$	$\vdots$	$\vdots$	$\vdots$	$\vdots$
12	$1.89{\cdot}10^{-5}$	$6.84{\cdot}10^{-13}$	$2.78{\cdot}10^{-5}$	$2.67{\cdot}10^{-12}$
13	$6.14{\cdot}10^{-12}$	$4.38{\cdot}10^{-26}$	$4.19{\cdot}10^{-7}$	$1.33{\cdot}10^{-12}$
14			$5.80{\cdot}10^{-7}$	$5.08{\cdot}10^{-15}$
15			$3.17{\cdot}10^{-8}$	$1.44{\cdot}10^{-15}$
16			$1.90{\cdot}10^{-8}$	$1.13{\cdot}10^{-17}$
17			$1.59{\cdot}10^{-9}$	$1.65{\cdot}10^{-18}$
18			$6.43{\cdot}10^{-10}$	$2.10{\cdot}10^{-20}$

5.2. T-shaped structure subject to bending and torsion

In this example a T-shaped structure shown in Figure 8 subject to bending and torsion is modelled. This structure is presented in [44] in the framework of the classical theory, and in [19] in the framework of the micropolar theory, which is the only geometrically non-linear numerical example without the material non-linearity effects solved using micropolar finite elements with large displacements and large rotations we have been able to find in the literature. In [19], however, only the deformed configurations for selected load steps are plotted, without any numerical results provided. The micropolar material parameters are here taken as in [19], i.e. $\mu = 10\ 500$ N/mm^2, $\lambda = 15\ 750$ N/mm^2, $\nu = 3\ 500$ N/mm^2, $\alpha = 0$ N, $\beta = 52.5$ N and $\gamma = 52.5$ N , which corresponds to the following engineering material parameters: $E = 27\ 300$ N/mm^2, $n = 0.3$, $N = 0.5$, $l_b = 0.05$ mm, $l_t = \sqrt{2}l_b$, $\psi = 1$. The rib of the structure is submitted to a resultant torsional moment M_1 at the free end and both ends of the flange are submitted to resultant bending moments M_2 chosen in the same proportion as in [19], i.e. $\frac{M_1}{M_2} = \frac{8}{15}$ while the material points in the plane where the rib touches the flange are completely fixed

$(u_1(x,1,z) = u_2(x,1,z) = u_3(x,1,z) = \varphi_1(x,1,z) = \varphi_2(x,1,z) = \varphi_3(x,1,z) = 0$, for $x \in [5,6]$ and $z \in [0,1]$). The problem is modelled using $M_1 = 600$ Nmm, $M_2 = 1125$ Nmm. The chosen values of the applied moments differ from the ones specified in [19] ($M_1 = 300\,000$ Nmm and $M_2 = 562\,500$ Nmm), which produce a deformation that is way above the theoretical predictions. The moments chosen here correspond to the ones defined in [44]. The resultant moments are assumed to follow from a constant distributed surface moment loads and are thus applied through corresponding concentrated nodal moments obtained by integration. The domain is discretised using 21 cube-shaped elements as shown in Figure 9. First the torsional load is applied in 20 equal load increments, keeping the flange free of any loading. Then, the two bending moments M_2 are applied at each end of the flange in another 20 equal load increments, while the torsional moment is kept constant. The displacements and microrotations at the nodes $P_1 = (0.0, 1.0, 1.0)$, $P_2 = (11.0, 1.0, 1.0)$, $P_3 = (5.0, 11.0, 1.0)$ and $P_4 = (6.0, 11.0, 1.0)$ obtained using both the Hex8NL and Hex27NL elements are shown in Tables 5 and 6. Note that the rotations of the points at the edges of the flange in the xy plane obtained using the Hex27NL elements are of the order of magnitude of the theoretical values $\dfrac{M_2 l}{EI}$ for $l = 5$ mm and $I = 0.8\dot{3}$ mm^4 in classical elasticity, while the rotations of the points at the edge of the rib around the y axis obtained using the same elements are in the order of magnitude of the theoretical values $\dfrac{M_1 L}{G I_t}$ for $L = 10$ mm, $G = \dfrac{E}{2(1+n)}$ and $I_t \approx 0.141$ mm^4. Note that the internal length-scales l_b and l_t amount to approximately 5-7% of the length of the square cross-section which justifies such a comparison with the results of classical elasticity. The Hex8NL mesh provides notably stiffer results.

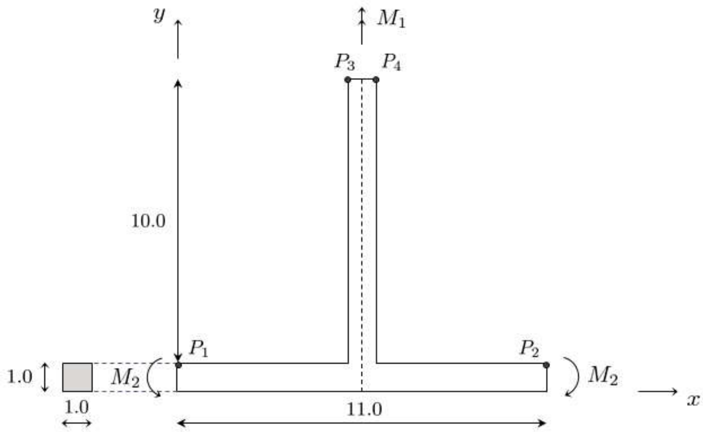

Figure 8: Top view of the T-shape structure [19]

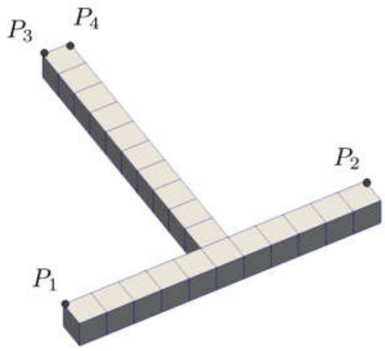

Figure 9: Finite element mesh of the T-shape structure

The various stages of deformation of the T-shape structure are presented in Figure 10 for Hex8NL and in Figure 11 for Hex27NL. We can see that the presented finite elements are able to model finite deformation problems, exhibiting large displacement and large rotations. No convergence problems are experienced even if the loading is doubled (see [22] for details).

Table 5: T-shaped structure subject to bending and torsion: Results obtained using $21 \times 1 \times 1$ Hex8NL elements in the last load step

Point	u_1	u_2	u_3	φ_1	φ_2	φ_3
P_1	1.2182	-3.6278	-1.1277 $\cdot 10^{-2}$	-1.4940 $\cdot 10^{-2}$	-5.2237 $\cdot 10^{-3}$	1.7303
P_2	-1.2182	-3.6278	-1.1277 $\cdot 10^{-2}$	-1.4940 $\cdot 10^{-2}$	5.2237 $\cdot 10^{-3}$	-1.7303
P_3	1.0335	2.7191 $\cdot 10^{-3}$	-9.7484 $\cdot 10^{-1}$	-4.5819 $\cdot 10^{-2}$	3.2176	-4.5027 $\cdot 10^{-2}$
P_4	-9.7484 $\cdot 10^{-1}$	2.7191 $\cdot 10^{-3}$	-1.0335	-4.5027 $\cdot 10^{-2}$	3.2176	4.5819 $\cdot 10^{-2}$

Table 6: T-shaped structure subject to bending and torsion: Results obtained using $21 \times 1 \times 1$ Hex27NL elements in the last load step

Point	u_1	u_2	u_3	φ_1	φ_2	φ_3
P_1	3.6130	-4.5842	-1.0906 $\cdot 10^{-2}$	-1.5587 $\cdot 10^{-2}$	-1.8711 $\cdot 10^{-2}$	3.0388
P_2	-3.6130	-4.5842	-1.0906 $\cdot 10^{-2}$	-1.5587 $\cdot 10^{-2}$	-1.8711 $\cdot 10^{-2}$	-3.0388
P_3	1.0051	-6.7156 $\cdot 10^{-3}$	-1.0078	-4.0736 $\cdot 10^{-2}$	3.4236	-4.2163 $\cdot 10^{-2}$
P_4	-1.0078	-6.7156 $\cdot 10^{-3}$	-1.0051	-4.2163 $\cdot 10^{-2}$	3.4236	4.0736 $\cdot 10^{-2}$

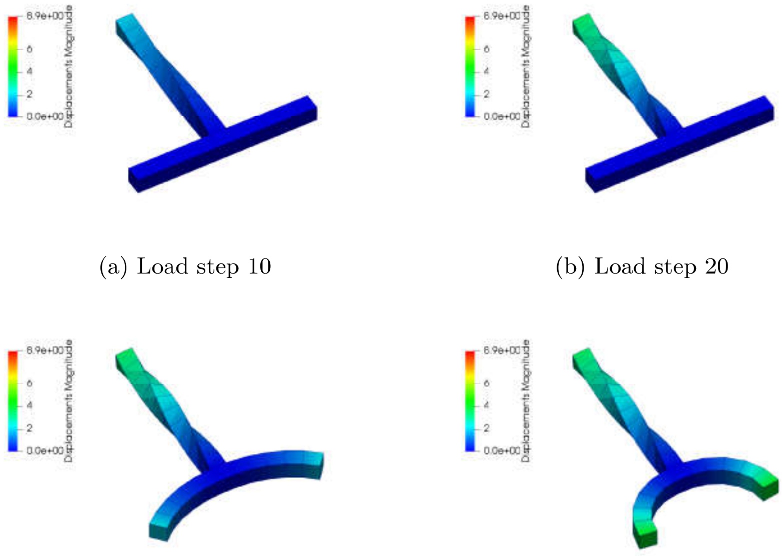

(a) Load step 10

(b) Load step 20

(c) Load step 30

(d) Load step 40

Figure 10: Deformed configuration of the T-shape structure for different load steps obtained using a mesh of $21 \times 1 \times 1$ Hex8NL elements

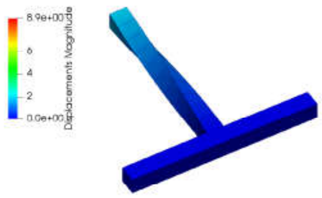

(a) Load step 10

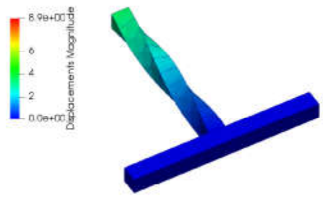

(b) Load step 20

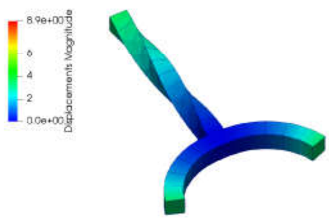

(c) Load step 30

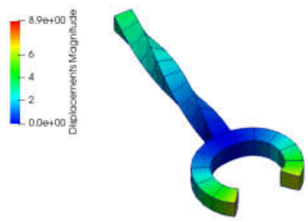

(d) Load step 40

Figure 11: Deformed configuration of the T-shape structure for different load steps obtained using a mesh of $21 \times 1 \times 1$ Hex27NL elements

In order to investigate the influence of parameter α on overall torsional stiffness of the rib, the problem is also solved by choosing $\alpha = 105$ N (corresponding to $\psi = 0.5$), while the remaining parameters, dimensions and mesh discretisation are kept as defined before. The obtained results using both elements are given in Tables 7 and 8 and do not differ much from the case with $\alpha = 0$ N, with only a slightly increased torsional stiffness of the rib observed.

Table 7: T-shaped structure subject to bending and torsion: Results obtained using $21 \times 1 \times 1$ Hex8NL elements in the last load step for $\alpha = 105$ N

Point	u_1	u_2	u_3	φ_1	φ_2	φ_3
P_1	1.2182	-3.6278	-1.1277 $\cdot 10^{-2}$	-1.4832 $\cdot 10^{-2}$	-5.2052 $\cdot 10^{-3}$	1.7303
P_2	-1.2182	-3.6278	-1.1277 $\cdot 10^{-2}$	-1.4832 $\cdot 10^{-2}$	5.2052 $\cdot 10^{-3}$	-1.7303
P_3	1.0357	2.3389 $\cdot 10^{-3}$	-9.7204 $\cdot 10^{-1}$	-5.0469 $\cdot 10^{-2}$	3.2077	-4.9839 $\cdot 10^{-2}$
P_4	-9.7204 $\cdot 10^{-1}$	2.3389 $\cdot 10^{-3}$	-1.0357	-4.9839 $\cdot 10^{-2}$	3.2077	5.0469 $\cdot 10^{-2}$

Table 8: T-shaped structure subject to bending and torsion: Results obtained using $21 \times 1 \times 1$ Hex27NL elements in the last load step for $\alpha = 105$ N

Point	u_1	u_2	u_3	φ_1	φ_2	φ_3
P_1	3.6128	-4.5840	-1.0810 $\cdot 10^{-2}$	-1.5482 $\cdot 10^{-2}$	-1.7621 $\cdot 10^{-2}$	3.0379
P_2	-3.6128	-4.5840	-1.0810 $\cdot 10^{-2}$	-1.5482 $\cdot 10^{-2}$	1.7621 $\cdot 10^{-2}$	-3.0379
P_3	1.0046	-4.9047 $\cdot 10^{-3}$	-1.0052	-5.9261 $\cdot 10^{-2}$	3.3900	-5.1069 $\cdot 10^{-2}$
P_4	-1.0052	-4.9047 $\cdot 10^{-3}$	-1.0046	-5.1069 $\cdot 10^{-2}$	3.3900	5.9261 $\cdot 10^{-2}$

5.3. 45° curved cantilever bend

In the previous two examples only predominantly two-dimensional problems have been analysed. To test the proposed formulation for genuine 3D behaviour involving large displacements and rotations we now analyse the well-known 45° bent cantilever of Bathe and Bolourchi [41]. However, no literature is found in which this problem has been modelled in the framework of 3D micropolar elasticity.

The cantilever lies in a horizontal plane and is curved by a radius of $R = 100$ for an angle of 45° (one eighth of a circle), as shown in Figure 12. The cantilever is loaded at the free end by a constant distributed surface loading in the x_3 direction $p_3 = 600$ along the square-shaped cross-section of the side $a = 1$. The distributed surface loading is applied through corresponding concentrated nodal forces obtained by integration in a number of load increments. The cantilever is clamped at the left-hand side end ($u_1(0, x_2, x_3) = u_2(0, x_2, x_3) = u_3(0, x_2, x_3) = \varphi_1(0, x_2, x_3) = \varphi_2(0, x_2, x_3) = \varphi_3(0, x_2, x_3) = 0$, for $x_2 \in [R - 0.5a, R + 0.5a]$, and $x_3 \in [0, a]$).

First, in order to compare the obtained results against a reference solution of the classical theory, Lamé constants are taken as in [44], i.e. $\mu = 5 \cdot 10^6$, $\lambda = 0$, while the micropolar parameters are taken as very small (but ν, β, γ necessarily larger than zero in order to satisfy the condition of the positiveness of strain energy). It is important to note that, as observed in all the numerical examples already analysed, the bigger the micropolar parameters are, the stiffer the structure is. Thus, even for small micropolar parameters, we expect a bit stiffer response than in the classical elasticity. The remaining material parameters are thus chosen as $\nu = 50\ 505.1$, $\alpha = 0$, $\beta = 12\ 500$ and $\gamma = 37\ 500$, which correspond to the following engineering material parameters: $E = 10^7$, $n = 0.0$, $N = 0.1$, $l_b = 0.05$, $l_t = 0.05$, $\psi = 1$. This problem is in [44] modelled by a mesh of 16 solid elements with 8 nodes enhanced by the incompatible modes. The results at nodes $P_1 = (70.357, 70.357, 0.0)$, $P_2 = (71.064, 71.064, 0.0)$, $P_3 = (70.357, 70.357, 1.0)$ and $P_4 = (71.064, 71.064, 1.0)$ are then averaged and the reference solution for the displacements u_1, u_2 and u_3 is given. Here, the obtained results using Hex8NL and Hex27NL elements for different mesh densities are compared against the results in [44] and presented in Table 9 for Hex8NL and in Table 10 for Hex27NL, where CPU time for both elements is also shown demonstrating high computational efficiency of Hex27NL. We can see that the results converge towards the results of [44] with both h- and p-refinement. The undeformed cantilever and its deformed state in the last load step obtained by 16 Hex27NL finite elements is shown in Figure 13.

We can see that the converged results for the finest meshes are very close to the results obtained using the classical theory of elasticity but, due to the presence of the micropolar effects, the structure is slightly stiffer, as expected. Also the elements with the order of interpolation comparable to that of the elements in [44] provide comparable solutions. As already observed in other numerical examples, the first order element Hex8NL shows poor results for coarse meshes, and it is likely that it may be improved by adding internal degrees of freedom.

To verify the Newton–Raphson solution procedure implemented, evolution of the residual and energy norms for one of the meshes analysed at a chosen load step is presented in Table 11.

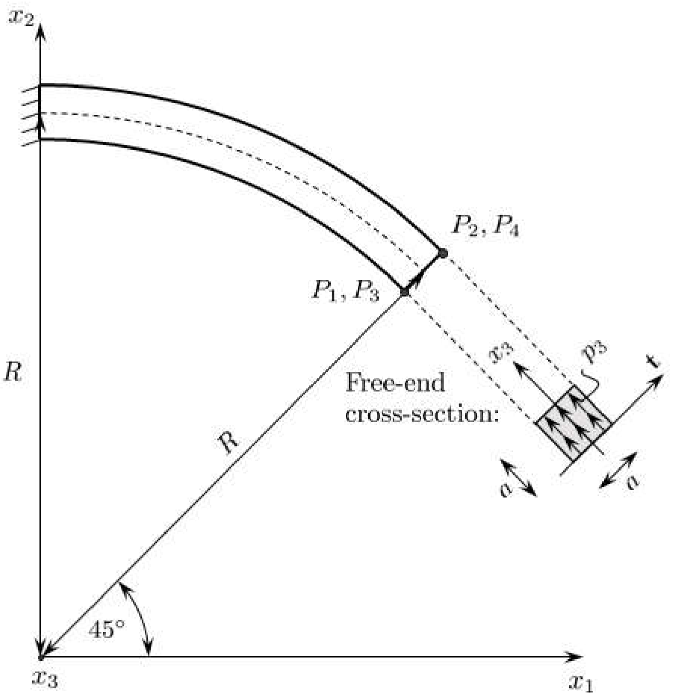

Figure 12: Top view of the curved cantilever beam and its loaded free-end cross-section

Table 9: 45° curved cantilever bend: Results obtained using Hex8NL elements

(a) $16 \times 1 \times 1$ Hex8NL elements (CPU time: 0.5s)

LS	Node	u_1	u_2	u_3
1	P_1	-1.28	1.91	16.06
	P_2	-1.24	1.80	15.76
	P_3	-1.32	2.40	15.93
	P_4	-1.28	2.29	15.63
Averaged results		-1.28	2.10	15.85
Ref. solution [44]		-23.30	13.64	53.21

(b) $128 \times 1 \times 1$ Hex8NL elements (CPU time: 1min 27s)

LS	Node	u_1	u_2	u_3
4	P_1	-19.60	11.38	50.21
	P_2	-19.72	11.46	50.40
	P_3	-20.35	11.83	49.69
	P_4	-20.47	11.91	49.89
Averaged results		-20.04	11.65	50.04
Ref. solution [44]		-23.30	13.64	53.21

(c) $256 \times 1 \times 1$ Hex8NL elements (CPU time: 26min 19s)

LS	Node	u_1	u_2	u_3
10	P_1	-21.53	12.48	52.20
	P_2	-21.68	12.58	52.42
	P_3	-22.32	12.91	51.64
	P_4	-22.48	13.00	51.85
Averaged results		-22.00	12.74	52.03
Ref. solution [44]		-23.30	13.64	53.21

*LS - number of load steps

Table 10: 45° curved cantilever bend: Results obtained using Hex27NL elements

(a) $6 \times 1 \times 1$ Hex27NL elements (CPU time: 12s)

LS	Node	u_1	u_2	u_3
5	P_1	-16.30	14.15	47.87
	P_2	-16.47	14.26	48.05
	P_3	-17.07	14.55	47.37
	P_4	-17.24	14.67	47.54
Averaged results		-16.77	14.50	47.63
Ref. solution [44]		-23.30	13.64	53.21

(b) $12 \times 1 \times 1$ Hex27NL elements (CPU time: 41s)

LS	Node	u_1	u_2	u_3
7	P_1	-21.60	12.94	52.31
	P_2	-21.77	13.05	52.53
	P_3	-22.40	13.36	51.74
	P_4	-22.57	13.47	51.95
Averaged results		-22.09	13.21	52.13
Ref. solution [44]		-23.30	13.64	53.21

(c) $16 \times 1 \times 1$ Hex27NL elements (CPU time: 1min 10s)

LS	Node	u_1	u_2	u_3
7	P_1	-22.05	12.85	52.70
	P_2	-22.22	12.96	52.92
	P_3	-22.86	13.27	52.12
	P_4	-23.03	13.37	52.34
Averaged results		-22.54	13.11	52.52
Ref. solution [44]		-23.30	13.64	53.21

*LS - number of load steps

Table 11: 45° curved cantilever bend: Convergence rate of the Newton–Raphson scheme for the mesh of 16 Hex27NL elements for load increment 6 ; residual and energy norms

Iteration	Residual norm	Energy norm
0	$4.28{\cdot}10^{1}$	$3.34{\cdot}10^{2}$
1	$5.05{\cdot}10^{5}$	$1.82{\cdot}10^{4}$
2	$3.64{\cdot}10^{2}$	$3.76{\cdot}10^{0}$
3	$4.98{\cdot}10^{3}$	$1.79{\cdot}10^{0}$
4	$5.21{\cdot}10^{-2}$	$1.21{\cdot}10^{-3}$
5	$5.89{\cdot}10^{-3}$	$2.26{\cdot}10^{-12}$
6	$1.16{\cdot}10^{-6}$	$3.66{\cdot}10^{-20}$

(a) No loading

(b) Load step 7

Figure 13: Undeformed and deformed configurations of the curved cantilever beam obtained using a mesh of $16 \times 1 \times 1$ Hex27NL elements

Next, we vary the micropolar material parameters and analyse the behavior of the structure for the finest mesh of Hex27NL elements (16 Hex27NL elements). First, the micropolar parameters μ, λ, α, β and γ are kept as previously defined and the value of the remaining parameter ν is varied so as to reflect the values of the coupling number $N \in \{0.1,\ 0.5,\ 0.9\}$ (N can have values between 0 and 1). The displacements at node P_1 are presented in Table 12. By increasing the value of the coupling number, the values of displacements reduce, even for $N = 0.9$ quite close results to the case with the smallest value of N are obtained, leading to the conclusion that N does not significantly affect the solution. Interestingly, the solution does become more robust with an increase in N, i.e. a converged solution has been obtained in fewer load steps.

Table 12: 45° curved cantilever bend: Displacements obtained using $16 \times 1 \times 1$ Hex27NL elements for different values of the coupling number N

LS	N	ν	u_1	u_2	u_3
7	0.1	50 505.05	-22.05	12.85	52.70
5	0.5	1 666 666.67	-21.89	12.76	52.55
5	0.9	21 315 789.47	-21.81	12.73	52.48

Next, we keep $\mu = 5 \cdot 10^6$, $\lambda = 0.$, $\nu = 50\ 505.1$, $\beta = 12\ 500$ and $\gamma = 37\ 500$ (which correspond to $E = 10^7$, $n = 0.0$, $l_b = 0.05$, $l_t = 0.05$, $N = 0.1$) and take different values of the polar ratio $\psi \in \{0.7,\ 1.0,\ 1.4\}$. The results are presented in Table 13.

Table 13: 45° curved cantilever bend: Displacements at node P_1 obtained using $16 \times 1 \times 1$ Hex27NL elements for different values of the polar ratio ψ

LS	ψ	α	u_1	u_2	u_3
7	0.7	10 714.3	-22.05	12.85	52.69
7	1.0	0.0	-22.05	12.85	52.70
7	1.4	-7142.86	-22.06	12.85	52.70

From Table 13 we can see that the influence of the increase in the polar ratio on the obtained numerical results is even more negligible than that of the coupling number.

Finally, we note that the interpolation of iterative changes of the rotation matrix necessarily produces a path-dependent solution (dependent on the number of load increments). As shown in [32], however, this anomalous behaviour reduces quickly with both h- and p-refinement. In 3D micropolar elasticity this is additionally attenuated by the fact that with lowest-order elements exceedingly fine meshes are needed to obtain an accurate result, while more pronounced micropolar effects make the response stiffer and thus less non-linear.

6. Conclusion

In this work deformation of the geometrically non-linear micropolar continuum is described in terms of Biot-like stress and strain tensors. After setting the weak form as a basis for the non-linear finite-element solution procedure, the residual load vector has been derived, linearised and updated with all the necessary algorithmic detail provided.

The actual discretisation has been performed using hexahedral finite elements interpolated using first- and second-order Lagrange interpolation and implemented within the Finite Element Analysis Program (FEAP) [39]. The elements have been tested on three non-linear problems: pure bending, combined bending and torsion and full 3D deformation. For the micropolar pure-bending test, an analytical reference solution is derived from the existing linear micropolar solution, and the elements are shown to converge towards this solution, with much better performance of the second-order element. Next, a micropolar T-shaped structure subject to bending and torsion is modelled, which is the only pure geometrically non-linear micropolar numerical example (without material non-linearity) we have been able to find in the literature [19]. The derived finite elements are able to model large displacements and large rotations and the obtained results are comparable to those obtained by the beam theory, again with an enhanced performance of the second-order element. Finally, a genuine three-dimensional problem, a curved cantilever subject to out-of-plane loading is modelled. The problem is modelled by taking very small micropolar parameters and the obtained results are shown to converge towards a reference solution of the classical theory with both h- and p-refinement. Owing to the micropolar effects, the material is slightly stiffer, which is actually observed in all the numerical examples analysed. A micropolar parameter sensitivity analysis is also performed within this example, where the values of the coupling number and polar ratio have been varied. It is concluded that none of those parameters affect the results significantly, but both of them increase the robustness of the solution procedure. The path dependence, typical of non-linear problems with large 3D rotational degrees of freedom and Lagrangian interpolation of rotational spins, is also present here, but it vanishes quickly with h- and p-refinement as well as with increase in micropolar effects.

Acknowledgement - This work has been financially supported by the Croatian Science Foundation research project *Fixed-Pole Concept in Numerical Modelling of Cosserats' Continuum* (HRZZ-IP-2018-01-1732) and the University of Rijeka research grant *Computational and Experimental Procedures for Assessment of Material Parameters in Cosserats' Continuum* (uniri-tehnic-18-248 1415) as well as the French Government scholarship for Sara Grbčić Erdelj.

AppendixA. Shape functions

The isoparametric shape functions for the Hex8NL element are defined as

$$N_i(\xi,\eta,\zeta)=\frac{1}{8}(1+\xi_a\xi)(1+\eta_a\eta)(1+\zeta_a\zeta),\ \ \xi_a=\pm1,\ \eta_a=\pm1,\ \zeta_a=\pm1,\ i=1,..,8, \tag{A.1}$$

and represent the Lagrange trilinear isoparametric shape functions [45]. For the Hex27NL element they are defined as [45]:

1. For vertex nodes:

$$N_i(\xi,\eta,\zeta)=\frac{1}{8}\xi\eta\zeta(1+\xi_a\xi)(1+\eta_a\eta)(1+\zeta_a\zeta), \tag{A.2}$$

2. For mid-edge nodes:

$$N_i=\frac{1}{4}\begin{cases}(1-\xi_a\xi)(1+\eta^2)(1+\zeta_a\zeta), & i=9,11,13,15,\\ (1-\xi^2)(1+\eta_a\eta)(1+\zeta_a\zeta), & i=10,12,14,16,\\ (1-\xi_a\xi)(1+\eta_a\eta)(1+\zeta^2), & i=17,18,19,20.\end{cases} \tag{A.3}$$

3. For mid-face nodes:

$$N_i=\frac{1}{2}\begin{cases}(1-\xi^2)(1-\eta^2)(1+\zeta_a\zeta), & i=21,22,\\ (1-\xi^2)(1+\eta_a\eta)(1-\zeta^2), & i=23,24,\\ (1+\xi_a\xi)(1-\eta^2)(1-\zeta^2), & i=25,26.\end{cases} \tag{A.4}$$

4. For the interior node

$$N_{27}=(1-\xi^2)(1-\eta^2)(1-\zeta^2). \tag{A.5}$$

AppendixB. Tensor identities

To facilitate derivation of the results in AppendixC some of the tensor-algebra identities used in this work are outlined here. The results can be confirmed by direct calculation, but also found in [46], [22].

Vectors:

The following identities hold for any 3D vectors $\mathbf{a}$ and $\mathbf{b}$:

$$\mathbf{a}\cdot\mathbf{b} = \mathbf{b}\cdot\mathbf{a} = \mathbf{a}^{\mathrm{T}}\mathbf{b} = \mathbf{b}^{\mathrm{T}}\mathbf{a}, \tag{B.1}$$

$$\mathbf{a}\otimes\mathbf{b} = \mathbf{a}\mathbf{b}^{\mathrm{T}}, \tag{B.2}$$

$$\mathbf{a}\times\mathbf{b} = \widehat{\mathbf{a}}\mathbf{b} = -\widehat{\mathbf{b}}\ \mathbf{a}, \tag{B.3}$$

$$\hat{\mathbf{a}}^{\mathrm{T}} = -\hat{\mathbf{a}}, \tag{B.4}$$

$$\mathbf{a} = -\frac{1}{2}\boldsymbol{\epsilon} : \hat{\mathbf{a}} = \mathrm{ax}(\hat{\mathbf{a}}), \tag{B.5}$$

$$\mathrm{tr}(\mathbf{a}\otimes\mathbf{b}) = \mathbf{a}\cdot\mathbf{b} = \mathbf{a}^{\mathrm{T}}\mathbf{b}, \tag{B.6}$$

$$\mathrm{tr}(\widehat{\mathbf{a}}\widehat{\mathbf{b}}) = -2\mathbf{a}\cdot\mathbf{b} = -2\mathbf{a}^{\mathrm{T}}\mathbf{b}, \tag{B.7}$$

$$\widehat{\mathbf{a}\times\mathbf{b}} = \mathbf{b}\otimes\mathbf{a} - \mathbf{a}\otimes\mathbf{b}, \tag{B.8}$$

$$\boldsymbol{\epsilon} : (\mathbf{a}\otimes\mathbf{b}) = -\widehat{\mathbf{b}}\mathbf{a} = \widehat{\mathbf{a}}\mathbf{b}. \tag{B.9}$$

where $\boldsymbol{\epsilon} = \epsilon_{ijk}\mathbf{e}_i\otimes\mathbf{e}_j\otimes\mathbf{e}_k$ for any right-handed orthonormal basis $\{\mathbf{e}_i\}$ and ϵ_{ijk} as the permutation symbol.

Tensors of order 2:

The following identities hold for any 3D 2nd order tensors $\mathbf{A},\ \mathbf{B},\ \mathbf{C}$:

$$\mathbf{A} : \mathbf{B} = \mathrm{tr}(\mathbf{A}\mathbf{B}^{\mathrm{T}}), \tag{B.10}$$

$$\mathbf{A} : \mathbf{B} = \mathbf{B} : \mathbf{A}, \tag{B.11}$$

$$\mathbf{A} : \mathbf{B}^{\mathrm{T}} = \mathbf{A}^{\mathrm{T}} : \mathbf{B}, \tag{B.12}$$

$$\mathrm{tr}(\mathbf{ABC}) = \mathrm{tr}(\mathbf{BCA}) = \mathrm{tr}(\mathbf{CAB}), \tag{B.13}$$

$$(\mathbf{ABC}) : \mathbf{D}^{\mathrm{T}} = (\mathbf{BCD}) : \mathbf{A}^{\mathrm{T}} = (\mathbf{CDA}) : \mathbf{B}^{\mathrm{T}}, \tag{B.14}$$

$$\mathrm{ax}(\mathbf{A} - \mathbf{A}^{\mathrm{T}}) = -\boldsymbol{\epsilon} : \mathbf{A} \tag{B.15}$$

$$\mathrm{ax}(\mathrm{skew}\mathbf{A}) = -\frac{1}{2}\boldsymbol{\epsilon} : \mathbf{A}, \tag{B.16}$$

$$\boldsymbol{\epsilon} : \mathbf{A} = -\boldsymbol{\epsilon} : \mathbf{A}^{\mathrm{T}} \tag{B.17}$$

$$\boldsymbol{\epsilon} : \left(\mathbf{A}\widehat{\mathbf{b}}\right) = \left(\mathbf{A}^{\mathrm{T}} - \mathrm{tr}(\mathbf{A})\mathbf{I}\right)\mathbf{b}, \tag{B.18}$$

$$\boldsymbol{\epsilon} : \left(\mathbf{A}\widehat{\mathbf{b}}\mathbf{A}\right) = -\left[\mathrm{ax}(2\mathrm{skew}(\mathbf{A}\widehat{\mathbf{E}_1}\mathbf{A}))\ \ \mathrm{ax}(2\mathrm{skew}(\mathbf{A}\widehat{\mathbf{E}_2}\mathbf{A}))\ \ \mathrm{ax}(2\mathrm{skew}(\mathbf{A}\widehat{\mathbf{E}_3}\mathbf{A}))\right]\mathbf{b}, \tag{B.19}$$

$$\text{with}\quad \mathbf{A} = A_{ij}\mathbf{E}_i \otimes \mathbf{E}_j. \tag{B.20}$$

Tensors of order 4:

$$\boldsymbol{\mathcal{I}} : \mathbf{A} = \mathbf{A} \tag{B.21}$$

$$\boldsymbol{\mathcal{I}}^{\mathrm{T}} : \mathbf{A} = \mathbf{A}^{\mathrm{T}} \tag{B.22}$$

AppendixC. Linearised residual $\Delta\mathbf{g}$

In order to linearise the nodal element residual $\mathbf{g}_i^e = \mathbf{q}_i^{int,e} - \mathbf{q}_i^{ext,e}$ with $\mathbf{q}_i^{int,e}$ given in (24) we concentrate on the integrands in $\Delta\mathbf{g}_i^e = \Delta\mathbf{q}_i^{int,e}$ in (30) explicitly given in (31). These are analysed in detail in AppendixC.1, AppendixC.2 and AppendixC.3. Before doing so let us note that the *linearised forms* of the strain and curvature tensors $\Delta\mathbf{E} = \left.\frac{\mathrm{d}}{\mathrm{d}\epsilon}\right|_{\epsilon=0} \mathbf{E}_\epsilon$ and $\Delta\mathbf{K} = \left.\frac{\mathrm{d}}{\mathrm{d}\epsilon}\right|_{\epsilon=0} \mathbf{K}_\epsilon$ with $\mathbf{E}$

and $\mathbf{K}$ given in (9) and (10) coincide in their form with the *virtual changes* of these tensors given in (8), which in fact have yielded (9) and (10) by integration. Therefore

$$\Delta\mathbf{E} = \mathbf{Q}^{\mathrm{T}}\left(\widehat{\Delta\boldsymbol{\varphi}}^{\mathrm{T}}\mathbf{F} + \mathrm{GRAD}\Delta\mathbf{u}\right), \tag{C.1}$$

$$\Delta\mathbf{K} = \mathbf{Q}^{\mathrm{T}}\mathrm{GRAD}\ \Delta\boldsymbol{\varphi}. \tag{C.2}$$

AppendixC.1. Term $\left(\widehat{\Delta\boldsymbol{\varphi}}\mathbf{QB} + \mathbf{Q}\left(\boldsymbol{\mathcal{T}} : \Delta\mathbf{E}\right)\right)\left(\nabla_X N_i\right)$

Term $\widehat{\Delta\boldsymbol{\varphi}}\mathbf{QB}(N_i\nabla_X)$ can be written as $-\widehat{\mathbf{QB}(N_i\nabla_X)}\Delta\boldsymbol{\varphi}$. For the term $\mathbf{Q}\left(\boldsymbol{\mathcal{T}} : \Delta\mathbf{E}\right)\left(N_i\nabla_X\right)$, we introduce (12) to obtain:

$$\begin{aligned}\mathbf{Q}\left(\boldsymbol{\mathcal{T}} : \Delta\mathbf{E}\right)\left(N_i\nabla_X\right) = {} & \lambda\mathbf{Q}\left(N_i\nabla_X\right)\mathrm{tr}(\Delta\mathbf{E}) + (\mu+\nu)\mathbf{Q}\Delta\mathbf{E}\left(N_i\nabla_X\right) \\ & + (\mu-\nu)\mathbf{Q}\Delta\mathbf{E}^{\mathrm{T}}\left(N_i\nabla_X\right).\end{aligned} \tag{C.3}$$

The three terms in (C.3) will be now analysed separately.

AppendixC.1.1. Term $\lambda\mathrm{tr}(\Delta\mathbf{E})\mathbf{Q}\left(N_i\nabla_X\right)$ *in (C.3)*

Using (C.1) we have

$$\mathrm{tr}(\Delta\mathbf{E}) = \mathrm{tr}\left(\mathbf{Q}^{\mathrm{T}}\widehat{\Delta\boldsymbol{\varphi}}^{\mathrm{T}}\mathbf{F}\right) + \mathrm{tr}\left(\mathbf{Q}^{\mathrm{T}}\mathrm{GRAD}\Delta\mathbf{u}\right), \tag{C.4}$$

and by using (B.13) and (B.7) we obtain

$$\mathrm{tr}\left(\mathbf{Q}^{\mathrm{T}}\widehat{\Delta\boldsymbol{\varphi}}^{\mathrm{T}}\mathbf{F}\right) = 2\left[\mathrm{ax}(\mathrm{skew}(\mathbf{F}\mathbf{Q}^{\mathrm{T}}))\right]^{\mathrm{T}}\Delta\boldsymbol{\varphi}, \tag{C.5}$$

since $\mathrm{tr}\left(\mathbf{F}\mathbf{Q}^{\mathrm{T}}\widehat{\Delta\boldsymbol{\varphi}}^{\mathrm{T}}\right) = \mathrm{tr}\left(\mathrm{symm}\left(\mathbf{F}\mathbf{Q}^{\mathrm{T}}\right)\widehat{\Delta\boldsymbol{\varphi}}^{\mathrm{T}}\right) + \mathrm{tr}\left(\mathrm{skew}\left(\mathbf{F}\mathbf{Q}^{\mathrm{T}}\right)\widehat{\Delta\boldsymbol{\varphi}}^{\mathrm{T}}\right) = -\mathrm{tr}\left(\mathrm{skew}\left(\mathbf{F}\mathbf{Q}^{\mathrm{T}}\right)\widehat{\Delta\boldsymbol{\varphi}}^{\mathrm{T}}\right)$. By using (B.6) and (B.2) we obtain

$$\mathrm{tr}\left(\mathbf{Q}^{\mathrm{T}}\mathrm{GRAD}\Delta\mathbf{u}\right) = \nabla_X^{\mathrm{T}}\mathbf{Q}^{\mathrm{T}}\Delta\mathbf{u}, \tag{C.6}$$

where ∇_X^{T} in (C.6) operates exclusively on $\Delta\mathbf{u}$. The first term in (C.3) thus follows as

$$\lambda \mathrm{tr}(\Delta\mathbf{E})\mathbf{Q}\left(N_i\nabla_X\right) = \Big(2\left[\mathrm{ax}(\mathrm{skew}(\mathbf{F}\mathbf{Q}^{\mathrm{T}}))\right]^{\mathrm{T}}\Delta\boldsymbol{\varphi} + \nabla_X^{\mathrm{T}}\mathbf{Q}^{\mathrm{T}}\Delta\mathbf{u}\Big)\lambda\mathbf{Q}\left(N_i\nabla_X\right). \tag{C.7}$$

AppendixC.1.2. Term $(\mu+\nu)\mathbf{Q}\Delta\mathbf{E}\left(N_i\nabla_X\right)$ in (C.3)

From (C.1), (B.4) and (B.3) we obtain

$$(\mu+\nu)\mathbf{Q}\Delta\mathbf{E}(N_i\nabla_X) = (\mu+\nu)\widehat{\mathbf{F}(N_i\nabla_X)}\Delta\boldsymbol{\varphi} + (\mu+\nu)\nabla_X^{\mathrm{T}}(N_i\nabla_X)\Delta\mathbf{u}, \tag{C.8}$$

where ∇_X^{T} in (C.8) operates exclusively on $\Delta\mathbf{u}$.

AppendixC.1.3. Term $(\mu-\nu)\mathbf{Q}\Delta\mathbf{E}^{\mathrm{T}}(N_i\nabla_X)$ in (C.3)

From (C.1), (B.1), (B.2) and (B.3) we obtain

$$\begin{aligned}(\mu-\nu)\mathbf{Q}\Delta\mathbf{E}^{\mathrm{T}}(N_i\nabla_X) &= -(\mu-\nu)\mathbf{Q}\mathbf{F}^{\mathrm{T}}\widehat{\mathbf{Q}(N_i\nabla_X)}\Delta\boldsymbol{\varphi}\\ &\quad + (\mu-\nu)\mathbf{Q}\nabla_X(N_i\nabla_X)^{\mathrm{T}}\mathbf{Q}^{\mathrm{T}}\Delta\mathbf{u},\end{aligned} \tag{C.9}$$

where ∇_X in (C.9) operates exclusively on $\Delta\mathbf{u}$. Substituting (C.7)-(C.9) in (C.3) and adding the result to $\widehat{\Delta\boldsymbol{\varphi}}\mathbf{Q}\mathbf{B}(N_i\nabla_X)$ we thus obtain

$$\begin{aligned}&\Big(\widehat{\Delta\boldsymbol{\varphi}}\mathbf{Q}\mathbf{B} + \mathbf{Q}\left(\boldsymbol{\mathcal{T}} : \Delta\mathbf{E}\right)\Big)\left(N_i\nabla_X\right)\\ &\quad= \left(\lambda\mathbf{Q}(N_i\nabla_X)\nabla_X^{\mathrm{T}}\mathbf{Q}^{\mathrm{T}} + (\mu+\nu)\nabla_X^{\mathrm{T}}(N_i\nabla_X)\mathbf{I} + (\mu-\nu)\mathbf{Q}\nabla_X(N_i\nabla_X)^{\mathrm{T}}\mathbf{Q}^{\mathrm{T}}\right)\Delta\mathbf{u}\\ &\quad+ \Big(-\widehat{\mathbf{Q}\mathbf{B}(N_i\nabla_X)} + \lambda\mathbf{Q}(N_i\nabla_X)2\left[\mathrm{ax}(\mathrm{skew}(\mathbf{F}\mathbf{Q}^{\mathrm{T}}))\right]^{\mathrm{T}} + (\mu+\nu)\widehat{\mathbf{F}(N_i\nabla_X)}\\ &\quad-(\mu-\nu)\mathbf{Q}\mathbf{F}^{\mathrm{T}}\widehat{\mathbf{Q}(N_i\nabla_X)}\Big)\Delta\boldsymbol{\varphi},\end{aligned} \tag{C.10}$$

where free ∇_X in the factor multiplying $\Delta\mathbf{u}$ operates only on $\Delta\mathbf{u}$.

AppendixC.2. Term $\left(\widehat{\Delta\boldsymbol{\varphi}}\mathbf{Q}\mathbf{G}+\mathbf{Q}\left(\boldsymbol{\mathcal{D}}:\Delta\mathbf{K}\right)\right)(N_i\nabla_X)$

The term $\widehat{\Delta\boldsymbol{\varphi}}\mathbf{Q}\mathbf{G}(N_i\nabla_X)$ can be written as $-\widehat{\mathbf{Q}\mathbf{G}(N_i\nabla_X)}\Delta\boldsymbol{\varphi}$. Following the same procedure as in AppendixC.1 we substitute (13) and obtain:

$$\begin{aligned}\mathbf{Q}\left(\boldsymbol{\mathcal{D}}:\Delta\mathbf{K}\right)(N_i\nabla_X) = {} & \alpha\mathbf{Q}(N_i\nabla_X)\mathrm{tr}(\Delta\mathbf{K})+(\beta+\gamma)\mathbf{Q}\Delta\mathbf{K}(N_i\nabla_X)\\ & +(\beta-\gamma)\mathbf{Q}\Delta\mathbf{K}^{\mathrm{T}}(N_i\nabla_X).\end{aligned} \tag{C.11}$$

AppendixC.2.1. Term $\alpha\mathrm{tr}(\Delta\mathbf{K})\mathbf{Q}(N_i\nabla_X)$ *in (C.11)*

From (C.2) and (B.6) we obtain

$$\alpha\mathrm{tr}(\Delta\mathbf{K})\mathbf{Q}(N_i\nabla_X)=\alpha\mathbf{Q}(N_i\nabla_X)\nabla_X^{\mathrm{T}}\mathbf{Q}^{\mathrm{T}}\Delta\boldsymbol{\varphi}, \tag{C.12}$$

where ∇_X^{T} in (C.12) operates only on $\Delta\boldsymbol{\varphi}$.

AppendixC.2.2. Term $(\beta+\gamma)\mathbf{Q}\Delta\mathbf{K}(N_i\nabla_X)$ *in (C.11)*

From (C.2), (B.2) and (B.1) we obtain

$$(\beta+\gamma)\mathbf{Q}\Delta\mathbf{K}(N_i\nabla_X)=(\beta+\gamma)\nabla_X^{\mathrm{T}}(N_i\nabla_X)\Delta\boldsymbol{\varphi}, \tag{C.13}$$

where ∇_X^{T} in (C.13) operates only on $\Delta\boldsymbol{\varphi}$.

AppendixC.2.3. Term $(\beta-\gamma)\mathbf{Q}\Delta\mathbf{K}^{\mathrm{T}}(N_i\nabla_X)$ *in (C.11)*

Analogously, we obtain

$$(\beta-\gamma)\mathbf{Q}\Delta\mathbf{K}^{\mathrm{T}}(N_i\nabla_X)=(\beta-\gamma)\mathbf{Q}\nabla_X(N_i\nabla_X)^{\mathrm{T}}\mathbf{Q}^{\mathrm{T}}\Delta\boldsymbol{\varphi}, \tag{C.14}$$

where ∇_X operates exclusively on $\Delta\boldsymbol{\varphi}$.

Substituting (C.12)-(C.14) in (C.11) and adding the term $\widehat{\Delta\boldsymbol{\varphi}}\mathbf{Q}\mathbf{G}(N_i\nabla_X)$ finally gives

$$\widehat{\Delta\boldsymbol{\varphi}}\mathbf{Q}\mathbf{G}(N_i\nabla_X) + \mathbf{Q}\left(\boldsymbol{\mathcal{D}} : \Delta\mathbf{K}\right)(N_i\nabla_X) = \Big(-\widehat{\mathbf{Q}\mathbf{G}(N_i\nabla_X)} + \alpha\mathbf{Q}(N_i\nabla_X)\nabla_X^{\mathrm{T}}\mathbf{Q}^{\mathrm{T}}$$
$$+ (\beta+\gamma)\nabla_X^{\mathrm{T}}(N_i\nabla_X)\mathbf{I} + (\beta-\gamma)\mathbf{Q}\nabla_X(N_i\nabla_X)^{\mathrm{T}}\mathbf{Q}^{\mathrm{T}}\Big)\Delta\boldsymbol{\varphi}. \tag{C.15}$$

AppendixC.3. Term $-N_i\boldsymbol{\epsilon} : \Big(\mathrm{GRAD}\Delta\mathbf{u}\mathbf{B}^{\mathrm{T}}\mathbf{Q}^{\mathrm{T}} + \left(\mathbf{F}(\boldsymbol{\mathcal{T}} : \Delta\mathbf{E})^{\mathrm{T}}\mathbf{Q}^{\mathrm{T}}\right) + \mathbf{F}\mathbf{B}^{\mathrm{T}}\mathbf{Q}^{\mathrm{T}}\widehat{\Delta\boldsymbol{\varphi}}^{\mathrm{T}}\Big)$

AppendixC.3.1. Term $-N_i\boldsymbol{\epsilon} : (\mathrm{GRAD}\Delta\mathbf{u}\mathbf{B}^{\mathrm{T}}\mathbf{Q}^{\mathrm{T}})$

By using (B.9), this term can be written as

$$-N_i\boldsymbol{\epsilon} : \left(\mathrm{GRAD}\Delta\mathbf{u}\mathbf{B}^{\mathrm{T}}\mathbf{Q}^{\mathrm{T}}\right) = N_i\widehat{\mathbf{Q}\mathbf{B}\nabla_X}\Delta\mathbf{u}, \tag{C.16}$$

where ∇_X in (C.16) operates exclusively on $\Delta\mathbf{u}$.

AppendixC.3.2. Term $-N_i\boldsymbol{\epsilon} : \left(\mathbf{F}(\boldsymbol{\mathcal{T}} : \Delta\mathbf{E})^{\mathrm{T}}\mathbf{Q}^{\mathrm{T}}\right)$

From (11), (C.1) and (C.4)-(C.6) we note that

$$(\boldsymbol{\mathcal{T}} : \Delta\mathbf{E})^{\mathrm{T}} = \lambda\ \mathrm{tr}(\Delta\mathbf{E})\mathbf{I} + (\mu+\nu)\Delta\mathbf{E}^{\mathrm{T}} + (\mu-\nu)\Delta\mathbf{E}, \tag{C.17}$$
$$\Delta\mathbf{E}^{\mathrm{T}} = \mathbf{F}^{\mathrm{T}}\widehat{\Delta\boldsymbol{\varphi}}\mathbf{Q} + \left[\mathrm{GRAD}(\Delta\mathbf{u})\right]^{\mathrm{T}}\mathbf{Q}, \tag{C.18}$$
$$\mathrm{tr}(\Delta\mathbf{E}) = 2\left[\mathrm{ax}(\mathrm{skew}(\mathbf{F}\mathbf{Q}^{\mathrm{T}}))\right]^{\mathrm{T}}\Delta\boldsymbol{\varphi} + \nabla_X^{\mathrm{T}}\mathbf{Q}^{\mathrm{T}}\Delta\mathbf{u}, \tag{C.19}$$

and obtain

$$-N_i\boldsymbol{\epsilon} : \left(\mathbf{F}(\boldsymbol{\mathcal{T}} : \Delta\mathbf{E})^{\mathrm{T}}\mathbf{Q}^{\mathrm{T}}\right) = -N_i\boldsymbol{\epsilon} : \left(\mathbf{F}(\lambda\ \mathrm{tr}(\Delta\mathbf{E})\mathbf{Q}^{\mathrm{T}}\right)$$
$$-N_i\boldsymbol{\epsilon} : \left(\mathbf{F}(\mu+\nu)\Delta\mathbf{E}^{\mathrm{T}}\mathbf{Q}^{\mathrm{T}}\right) - N_i\boldsymbol{\epsilon} : \left(\mathbf{F}(\mu-\nu)\Delta\mathbf{E}\mathbf{Q}^{\mathrm{T}}\right). \tag{C.20}$$

By using (B.16), the first term in (C.20) can be written as:

$$-N_i\boldsymbol{\epsilon} : \left(\mathbf{F}(\lambda\ \mathrm{tr}(\Delta\mathbf{E})\mathbf{I}\mathbf{Q}^{\mathrm{T}}\right) = 4\lambda N_i\ \mathrm{ax}(\mathrm{skew}(\mathbf{F}\mathbf{Q}^{\mathrm{T}}))\left[\mathrm{ax}(\mathrm{skew}(\mathbf{F}\mathbf{Q}^{\mathrm{T}}))\right]^{\mathrm{T}}\Delta\boldsymbol{\varphi}$$
$$+ 2\lambda N_i\ \mathrm{ax}(\mathrm{skew}(\mathbf{F}\mathbf{Q}^{\mathrm{T}}))\nabla_X^{\mathrm{T}}\mathbf{Q}^{\mathrm{T}}\Delta\mathbf{u}. \tag{C.21}$$

Using (C.18), the second term in (C.20) can be written as

$$-N_i\boldsymbol{\epsilon} : \left(\mathbf{F}(\mu+\nu)\Delta\mathbf{E}^{\mathrm{T}}\mathbf{Q}^{\mathrm{T}}\right) = -\,(\mu+\nu)N_i\boldsymbol{\epsilon} : \left(\mathbf{F}\mathbf{F}^{\mathrm{T}}\widehat{\Delta\boldsymbol{\varphi}}\right) \\ -\,(\mu+\nu)N_i\boldsymbol{\epsilon} : \left(\mathbf{F}\left[\mathrm{GRAD}\Delta\mathbf{u}\right]^{\mathrm{T}}\right), \tag{C.22}$$

where

$$-(\mu+\nu)N_i\boldsymbol{\epsilon} : \left(\mathbf{F}\mathbf{F}^{\mathrm{T}}\widehat{\Delta\boldsymbol{\varphi}}\right) = -(\mu+\nu)N_i\left(\mathbf{F}\mathbf{F}^{\mathrm{T}} - \mathrm{tr}(\mathbf{F}\mathbf{F}^{\mathrm{T}})\mathbf{I}\right)\Delta\boldsymbol{\varphi}, \tag{C.23}$$

and

$$-(\mu+\nu)N_i\boldsymbol{\epsilon} : \left(\mathbf{F}\left[\mathrm{GRAD}\Delta\mathbf{u}\right]^{\mathrm{T}}\right) = -(\mu+\nu)N_i\widehat{\mathbf{F}\nabla_X}\Delta\mathbf{u}, \tag{C.24}$$

owing to (B.18) and (B.9). Therefore

$$-N_i\boldsymbol{\epsilon} : \left(\mathbf{F}(\mu+\nu)\Delta\mathbf{E}^{\mathrm{T}}\mathbf{Q}^{\mathrm{T}}\right) = -(\mu+\nu)N_i\left(\mathbf{F}\mathbf{F}^{\mathrm{T}} - \mathrm{tr}(\mathbf{F}\mathbf{F}^{\mathrm{T}})\mathbf{I}\right)\Delta\boldsymbol{\varphi} \\ -\,(\mu+\nu)N_i\widehat{\mathbf{F}\nabla_X}\Delta\mathbf{u}. \tag{C.25}$$

Using (C.1), the third term in (C.20) may be written as

$$-N_i\boldsymbol{\epsilon} : \left(\mathbf{F}(\mu-\nu)\Delta\mathbf{E}\mathbf{Q}^{\mathrm{T}}\right) = -(\mu-\nu)N_i\boldsymbol{\epsilon} : \left(\mathbf{F}\mathbf{Q}^{\mathrm{T}}\widehat{\Delta\boldsymbol{\varphi}}^{\mathrm{T}}\mathbf{F}\mathbf{Q}^{\mathrm{T}}\right) \\ -\,(\mu-\nu)N_i\boldsymbol{\epsilon} : \left(\mathbf{F}\mathbf{Q}^{\mathrm{T}}\mathrm{GRAD}\Delta\mathbf{u}\mathbf{Q}^{\mathrm{T}}\right), \tag{C.26}$$

where

$$-(\mu-\nu)N_i\boldsymbol{\epsilon} : \left(\mathbf{F}\mathbf{Q}^{\mathrm{T}}\widehat{\Delta\boldsymbol{\varphi}}^{\mathrm{T}}\mathbf{F}\mathbf{Q}^{\mathrm{T}}\right) = (\mu-\nu)N_i\left[\widehat{\mathbf{m_1}}\quad\widehat{\mathbf{m_2}}\quad\widehat{\mathbf{m_3}}\right]\Delta\boldsymbol{\varphi}$$

with $\mathbf{m_i} = -\mathrm{ax}(2\mathrm{skew}(\mathbf{F}\mathbf{Q}^{\mathrm{T}}\widehat{\mathbf{E}_i}\mathbf{F}\mathbf{Q}^{\mathrm{T}}))$ and

$$-(\mu-\nu)N_i\boldsymbol{\epsilon} : \left(\mathbf{F}\mathbf{Q}^{\mathrm{T}}\mathrm{GRAD}(\Delta\mathbf{u})\mathbf{Q}^{\mathrm{T}}\right) = (\mu-\nu)N_i\widehat{\mathbf{Q}\nabla_X}\mathbf{F}\mathbf{Q}^{\mathrm{T}}\Delta\mathbf{u}, \qquad \text{(C.27)}$$

owing to (B.19) and (B.9), i.e.

$$-N_i\boldsymbol{\epsilon} : \left(\mathbf{F}(\mu-\nu)\Delta\mathbf{E}\mathbf{Q}^{\mathrm{T}}\right) = (\mu-\nu)N_i\widehat{\mathbf{Q}\nabla_X}\mathbf{F}\mathbf{Q}^{\mathrm{T}}\Delta\mathbf{u} + (\mu-\nu)N_i\left[\widehat{\mathbf{m_1}} \;\; \widehat{\mathbf{m_2}} \;\; \widehat{\mathbf{m_3}}\right]\Delta\boldsymbol{\varphi}. \qquad \text{(C.28)}$$

AppendixC.3.3. Term $-N_i\boldsymbol{\epsilon} : \left(\mathbf{F}\mathbf{B}^{\mathrm{T}}\mathbf{Q}^{\mathrm{T}}\widehat{\Delta\boldsymbol{\varphi}}^{\mathrm{T}}\right)$

By applying (B.18) we obtain:

$$-N_i\boldsymbol{\epsilon} : \left(\mathbf{F}\mathbf{B}^{\mathrm{T}}\mathbf{Q}^{\mathrm{T}}\widehat{\Delta\boldsymbol{\varphi}}^{\mathrm{T}}\right) = N_i\left[\left(\mathbf{F}\mathbf{B}^{\mathrm{T}}\mathbf{Q}^{\mathrm{T}}\right)^{\mathrm{T}} - \mathrm{tr}\left(\mathbf{F}\mathbf{B}^{\mathrm{T}}\mathbf{Q}^{\mathrm{T}}\right)\mathbf{I}\right]\Delta\boldsymbol{\varphi}. \qquad \text{(C.29)}$$

Summing up the contributions from (C.16), (C.21), (C.25), (C.28) and (C.29) we finally obtain

$$\begin{aligned}
&- N_i\boldsymbol{\epsilon} : \left(\mathrm{GRAD}\Delta\mathbf{u}\mathbf{B}^{\mathrm{T}}\mathbf{Q}^{\mathrm{T}} + \mathbf{F}\left(\mathcal{T} : \Delta\mathbf{E}\right)^{\mathrm{T}}\mathbf{Q}^{\mathrm{T}} + \mathbf{F}\mathbf{B}^{\mathrm{T}}\mathbf{Q}^{\mathrm{T}}\widehat{\Delta\boldsymbol{\varphi}}^{\mathrm{T}}\right) \\
&= N_i\widehat{\mathbf{Q}\mathbf{B}\nabla_X}\Delta\mathbf{u} + 4\lambda N_i\ \mathrm{ax}(\mathrm{skew}(\mathbf{F}\mathbf{Q}^{\mathrm{T}}))\left[\mathrm{ax}(\mathrm{skew}(\mathbf{F}\mathbf{Q}^{\mathrm{T}}))\right]^{\mathrm{T}}\Delta\boldsymbol{\varphi} \\
&+ 2\lambda N_i\ \mathrm{ax}(\mathrm{skew}(\mathbf{F}\mathbf{Q}^{\mathrm{T}}))\nabla_X^{\mathrm{T}}\mathbf{Q}^{\mathrm{T}}\Delta\mathbf{u} - (\mu+\nu)N_i\left(\mathbf{F}\mathbf{F}^{\mathrm{T}} - \mathrm{tr}(\mathbf{F}\mathbf{F}^{\mathrm{T}})\mathbf{I}\right)\Delta\boldsymbol{\varphi} \\
&- (\mu+\nu)N_i\widehat{\mathbf{F}\nabla_X}\Delta\mathbf{u} + (\mu-\nu)N_i\left[\widehat{\mathbf{m_1}} \;\; \widehat{\mathbf{m_2}} \;\; \widehat{\mathbf{m_3}}\right]\Delta\boldsymbol{\varphi} \\
&+ (\mu-\nu)N_i\widehat{\mathbf{Q}\nabla_X}\mathbf{F}\mathbf{Q}^{\mathrm{T}}\Delta\mathbf{u} + N_i\left[\left(\mathbf{F}\mathbf{B}^{\mathrm{T}}\mathbf{Q}^{\mathrm{T}}\right)^{\mathrm{T}} - \mathrm{tr}\left(\mathbf{F}\mathbf{B}^{\mathrm{T}}\mathbf{Q}^{\mathrm{T}}\right)\mathbf{I}\right]\Delta\boldsymbol{\varphi},
\end{aligned}$$

where $\mathbf{m_i} = -\mathrm{ax}(2\mathrm{skew}(\mathbf{F}\mathbf{Q}^{\mathrm{T}}\widehat{\mathbf{E}_i}\mathbf{F}\mathbf{Q}^{\mathrm{T}}))$ and all ∇_X operate on $\Delta\mathbf{u}$.

References

[1] E. Cosserat and F. Cosserat. *Théorie des corps déformables.* Herman, Paris, 1909.

[2] J. Dyszlewicz. *Micropolar Theory of Elasticity.* Springer-Verlag Berlin and Heidelberg GmbH & Co. KG, Berlin, 2004.

[3] A. C. Eringen. *Microcontinuum Field Theories: I. Foundations and Solids.* Springer-Verlag, New York, 2012.

[4] V.A. Eremeyev, L.P. Lebedev, and H. Altenbach. *Foundations of Micropolar Mechanics*. Springer-Verlag, Berlin, 2013.

[5] E. Providas and M. A. Kattis. Finite element method in plane Cosserat elasticity. *Computers and Structures*, 80(27-30):2059–2069, 2002.

[6] F.-Y. Huang and K.-Z. Liang. Torsional Analysis of micropolar elasticity using the finite element method. *International Journal of Engineering Science*, 32(2):347–358, 1994.

[7] F.-Y. Huang, B.-H. Yan, J.-L. Yan, and D.-U. Yang. Bending analysis of micropolar elastic beam using a 3-D finite element method. *International Journal of Engineering Science*, 38:275–286, 2000.

[8] L. Li and S. Xie. Finite element method for linear micropolar elasticity and numerical study of some scale effects phenomena in MEMS. *International Journal of Mechanical Sciences*, 46(11):1571–1587, 2004.

[9] H. Zhang, H. Wang, and G. Liu. Quadrilateral isoparametric finite elements for plane elastic Cosserat bodies. *Acta Mechanica Sinica*, 21(4):388–394, 2005.

[10] V. V. Korepanov, V. P. Matveenko, and I. N. Shardakov. Finite element analysis of two- and three-dimensional static problems in the asymmetric theory of elasticity as a basis for the design of experiments. *Acta Mechanica*, 223(8):1739–1750, 2012.

[11] M. A. Wheel. A control volume-based finite element method for plane micropolar elasticity. *International Journal for Numerical Methods in Engineering*, 75(8):992–1006, 2008.

[12] A. J. Beveridge, M. A. Wheel, and D. H. Nash. A higher order control volume based finite element method to predict the deformation of heterogeneous materials. *Comput. Struct.*, 129:54–62, 2013.

[13] S. Grbčić, A. Ibrahimbegović, and G. Jelenić. Variational formulation of micropolar elasticity using 3D hexahedral finite-element interpolation with incompatible modes. *Computers and Structures*, 205:1–14, 2018.

[14] S. Grbčić, G. Jelenić, and D. Ribarić. Quadrilateral 2D linked-interpolation finite elements for micropolar continuum. *Acta Mechanica Sinica*, 5(35):1001–1020, 2019.

[15] P. Steinmann and E. Stein. A unifying treatise of variational principles for two types of micropolar continua. *Acta Mechanica*, 121(1-4):215–232, 1997.

[16] W. Pietraszkiewicz and V . A. Eremeyev. On vectorially parameterized natural strain measures of the non-linear Cosserat continuum. *International Journal of Solids and Structures*, 46(11-12):2477–2480, 2009.

[17] W. Pietraszkiewicz and V. A. Eremeyev. On natural strain measures of the non-linear micropolar continuum. *International Journal of Solids and Structures*, 46(3-4):774–787, 2009.

[18] Paul Steinmann. A micropolar theory of finite deformation and finite rotation multiplicative elastoplasticity. *International Journal of Solids and Structures*, 31(8):1063–1084, 1994.

[19] S. Bauer, M. Schäfer, P. Grammenoudis, and Ch. Tsakmakis. Three-dimensional finite elements for large deformation micropolar elasticity. *Computer Methods in Applied Mechanics and Engineering*, 199(41-44):2643–2654, 2010.

[20] S. Bauer, W. G. Dettmer, D. Peric, and M. Schäfer. Micropolar hyperelasticity: constitutive model, consistent linearization and simulation of 3D scale effects. *Computational Mechanics*, 50:383–396, 2012.

[21] S. Bauer, W. G. Dettmer, D. Peric, and M. Schäfer. Micropolar hyper-elastoplasticity: constitutive model, consistent linearization, and simulation of 3D scale effects. *International Journal for Numerical Methods in Engineering*, 91:39–66, 2012.

[22] S. Grbčić. *Linked interpolation and strain invariance in finite-element modelling of micropolar continuum.* Phd thesis, University of Rijeka and Université de Technologie de Compiègne Sorbonne Universités, 2018.

[23] P. Grammenoudis and Ch. Tsakmakis. Finite element implementation of large deformation micropolar plasticity exhibiting isotropic and kinematic hardening effects. *Int. J. Numer. Meth. Engng*, 62:1691–1720, 2005.

[24] S. Ramezani, R. Naghdabadi, and S. Sohrabpour. Non-linear finite element implementation of micropolar hypo-elastic materials. *Computer Methods in Applied Mechanics and Engineering*, 197:4149–4159, 2008.

[25] A. Ibrahimbegović. *Nonlinear Solid Mechanics: Theoretical Formulations and Finite Element Solution Methods.* Springer, London, 2009.

[26] B. Hall. *Lie Grups, Lie Algebras, and representations: An Elementary Introduction.* Springer-Verlag, New York, 2003.

[27] L. E. Malvern. *Introduction to the mechanics of a continious medium.* Prentice-Hall, Inc, New Jersey, 1969.

[28] H. Jeffreys and B. Jeffreys. Change of Variables in an Integral. In *Methods of Mathematical Physics*, pages 32–33. Cambridge University Press, Cambridge, 3rd edition, 1988.

[29] E. Reissner. On one-dimensional finite-strain beam theory: The plane problem. *Zeitschrift für angewandte Mathematik und Physik ZAMP*, 23(5):795–804, sep 1972.

[30] J. C. Simo. A finite strain beam formulation. The three-dimensional dynamic problem. Part I. *Computer Methods in Applied Mechanics and Engineering*, 31(49):55–70, 1985.

[31] R. A. Toupin. Theories of elasticity with couple-stress. *Archive for Rational Mechanics and Analysis*, 17(2):85–112, 1964.

[32] G. Jelenić and M.A. Crisfield. Geometrically exact 3D beam theory: implementation of a strain-invariant finite element for statics and dynamics. *Computer Methods in Applied Mechanics and Engineering*, 171(1-2):141–171, 1999.

[33] J. Argyris. An excursion into large rotations. *Computer Methods in Applied Mechanics and Engineering*, 32(1-3):85–155, sep 1982.

[34] H. Goldstein, C.P. Poole, and J.L. Safko. *Classical Mechanics*. Addison-Wesley, San Francisco, 3rd edition, 2001.

[35] A. Ibrahimbegovic. On the choice of finite rotation parameters. *Computer Methods in Applied Mechanics and Engineering*, 149(1-4):49–71, 1997.

[36] A. Ibrahimbegovic and I. Kozar. Non-linear Wilson's brick element for finite elastic deformations of three-dimensional solids. *Communications in Numerical Methods in Engineering*, 11(8):655–664, 1995.

[37] A. Ibrahimbegović, I. Kožar, and F. Frey. Computational Aspects of Vector-Like Parametrization of Three-Dimensional Finite Rotations. *International Journal for Numerical Methods in Engineering*, 38:3653–3673, 1995.

[38] M. Gaćeša. *Fixed-Pole Concept in 3D Beam Finite Elements - Relationship to Standard Approaches and Analysis of Different Interpolations*. PhD thesis, University of Rijeka, Faculty of Civil Engineering, 2015.

[39] R.L. Taylor. FEAP - Finite Element Analysis Program, 2014.

[40] R.D. Gauthier and W. E. Jahsman. A Quest for Micropolar Elastic Constants. *Journal of Applied Mechanics*, 42(2):369–374, 1975.

[41] K. J. Bathe and S. Bolourchi. Large displacement analysis of three-dimensional beam structures. *International Journal for Numerical Methods in Engineering*, 14(7):961–986, jan 1979.

[42] M. Gaćeša and G. Jelenić. Modified fixed-pole approach in geometrically exact spatial beam finite elements. *Finite Elements in Analysis and Design*, 99:39–48, 2015.

[43] A. Ibrahimbegović and R.L. Taylor. On the role of frame-invariance in structural mechanics models at finite rotations. *Computer Methods in Applied Mechanics and Engineering*, 191:5159–5176, 2002.

[44] I. Kožar and A. Ibrahimbegović. Finite element formulation of the finite rotation solid element. *Finite Elements in Analysis and Design*, 20(2):101–126, jun 1995.

[45] O. C. Zienkiewicz and R. L. Taylor. *The Finite Element Method Volume 1 : The Basis*. Butterworth-Heinemann, Oxford, 2000.

[46] R. W. Ogden. *Non-Linear Elastic Deformations*. Dover Publications, Inc., Mineola, New York, 2013.